Supplementary Information (SI) for Energy & Environmental Science.
This journal is © The Royal Society of Chemistry 2024

SUPPORTING INFORMATION for:

Film-forming polymer nanoparticle strategy for improving the passivation and stability of perovskite solar cells

Zhenyu Jia[a,*], Ran Wang[a], Lei Zhu[b], Amal Altujjar[a,c], Polina Jacoutot[d], Osama M. Alkhudhari[a,e], Muhamad Z. Mokhtar[a,f], Ben F. Spencer[a,g], Nigel W. Hodson[h], Xuelian Wang[a], Mollie Osborne-Richards[a], Andrew G. Thomas[a,g], Teruo Hashimoto[a], Michael Faulkner[a], David J. Lewis[a], Saif. A. Haque[d], M. Saiful Islam[b], Jennifer M. Saunders[a] and Brian R. Saunders[a,*]

a) *Department of Materials, University of Manchester, Engineering Building A, Manchester, M1 7HL, U.K.*

b) *Department of Materials, University of Oxford, Oxford, OX1 3PH, UK.*

c) *Basic Science Department, Deanship of Preparatory Year and Supporting Studies, Imam Abdulrahman Bin Faisal University, Dammam 34221, KSA.*

d) *Department of Chemistry, Imperial College London, Molecular Sciences Research Hub, Wood Lane, W12 0BZ, UK.*

e) *Department of Chemistry, Taif University, Taif, 21974, Saudi Arabia.*

f) *Department of Water and Environmental Engineering, M46, Faculty of Civil Engineering, Universiti Teknologi Malaysia, 81310, Johor Bahru, Malaysia.*

g) *Photon Science Institute, The Henry Royce Institute, University of Manchester, Manchester, M13 9PL, UK*

h) *BioAFM Facility, Faculty of Biology, Medicine and Health, Stopford Building, University of Manchester, Oxford Road, Manchester, M13 9PT, UK.*

EXPERIMENTAL DETAILS

Materials.

Ethyleneglycol dimethacrylate (EGDMA, 98%), 2-(2-methoxyethoxy) ethylmethacrylate) (MEO_2MA, 98%), sodium dodecyl sulfate (SDS, ≥ 98.5%), potassium persulfate (KPS, ≥ 99.0%), 2-methoxy ethanol (95%), titanium isopropoxide (≥ 97.0%), ethanolamine (≥ 98%), methylammonium chloride (MACl, ≥ 98%), 2,2',7,7'-tetrakis[*N*,*N*-di(4-methoxyphenyl)amino]-9,9'-spirobifluorene (Spiro-OMeTAD, > 99.5%), lithium bis(trifluoromethylsulphonyl) imide (LiTFSI, 99.99%) DMF (99.8%), dimethyl sulfoxide (DMSO, 99.9%), chlorobenzene (CBZ, 99.8%), Co (III) TFSI salt (FK 209, ≥ 98%), acetonitrile (ACN, >99.9%) and 4-tert-butylpyridine (*t*-BP, ≥ 98%) were all purchased from Sigma-Aldrich. ITO coated glass (20 mm x 15 mm x 1.1 mm, unpatterned), Hellmanex III, methylammonium Iodide (MAI, ≥ 98%) and formamidinium Iodide (FAI, >99.5) were purchased from Ossila Limited. Lead (II) iodide (PbI_2, 99.9%) was purchased from Tokyo Chemical Industry UK Ltd. All materials and chemicals were used as received. Water was of ultrahigh purity and deionized.

Nanogel synthesis

Each of the nanogels was synthesized using similar methods. An example synthesis is described for NG-100. SDS (60 mg) was dissolved in water (200 mL) contained within a round bottom flask with lid, stirrer with blade and a reflux condenser. The solution was heated to 70 °C and stirred mechanically under a N_2 atmosphere. After 60 min, MEO_2MA (2.81 g, 14.3 mmol), EGDMA (0.030 g, 0.156 mmol) and then an aqueous solution of KPS (60 mg in 12.0 mL water) were added. The polymerization was continued for 6 h. The dispersion was cooled to room temperature and filtered through a 53 μm copper sieve. The dispersion was dialyzed against water for 10 days. The water for dialysis was changed 2 times per day over a 10-day period. To transfer the nanogel from water to DMF, the nanogel particles in water were centrifuged and then redispersed in DMF to obtain a 30 mg/g nanogel dispersion in DMF solution. Similar preparation methods were used for NG-60 and

NG-200 using different reactant masses and stirrer blades. The masses of the reactants used for the NG-60, NG-100 and NG-200 nanogel preparations, as well as the other details, are given in Table S1.

Perovskite film preparation

The ITO coated glass substrates (20 Ω/sq) were cleaned by ultrasonication in water, followed by ethanol, acetone, IPA and Hellmanex solution. After drying, the substrates were cleaned by UV-Ozone for 15 min. Then, a TiO_2 electron transport layer was spin-coated at 5000 rpm for 30 s onto the ITO using a mixture of 2-methoxy ethanol (95%, 2000 μL), titanium isopropoxide (160 μL) and ethanolamine (140 μL) and the TiO_2 layer was annealed at 450 °C for 30 min with step-by-step annealing. This involved the temperature being increased from room temperature to 125°C and holding for 5 minutes, followed by an increase to 325°C for another 5 minutes, and then a further increase to 450°C for 30 minutes. After cooling to the room temperature, the glass/ITO/TiO_2 substrates were then transferred to a glove box (RH ~ 8%).

All the following operations were carried out in the glove box. The perovskite films were prepared using a precursor solution containing MACl, MAI, FAI and PbI_2 in a mixture of DMF and DMSO (volume ratio 4:1). An example is given for a perovskite film prepared using 3.0 mg/g of NG-100. The perovskite precursor solution contained MACl (0.015 g, 0.22 mmol), MAI (0.037 g, 0.23 mmol), FAI (0.12 g, 0.70 mmol) and PbI_2 (0.461 g, 1.0 mmol) in a mixture of DMF with NG-100 solution (0.127 g, 30 mg/g), DMF (0.364 g) and DMSO (0.143 g). The nominal perovskite composition is $FA_{0.75}MA_{0.25}PbI_3$. The mixed solution was heated at 50 °C for 90 min with vigorous stirring before deposition. After cooling to room temperature, the precursor solution containing nanogel (100 μL) was spin-coated onto ITO/TiO_2 substrate at 1000 rpm for 10 s and then 4000 rpm for 40 s. During the spin coating process, CBZ (200 μL) was dripped onto the surface over 1 s at the end of the last 15 s. The films were then annealed at 100 °C for 50 min. Details of all the precursor solution compositions used to prepare the perovskite films in this study are given in Table S3.

Device construction

Device construction, including Spiro-OMeTAD deposition, was conducted inside a nitrogen-filled glovebox (humidity ~ 8%). Spiro-OMeTAD (90 mg) was added into CBZ (1.0 mL) with *t*-BP (34 µL), LiTFSI (19 µL, 520 mg/L) and FK 209 (10 µL) and heated at 45 °C with stirring for 10 min. Then, the solution was filtered (0.22 µm, Fisherbrand™). After that, Spiro (80 µL) precursor was deposited on the perovskite layer at 4000 rpm for 30 s by a dynamic spin coating. The planar devices were coated with a gold layer (80 nm) using thermal evaporation.

Physical measurements

Dynamic light scattering (DLS) measurements were conducted using a Malvern Zetasizer Nano ZS instrument and provide the z-average diameter (d_z). Zeta potential data were obtained using the same instrument. Samples for zeta potential used water as the solvent. SEM images were obtained using a ZEISS Ultra-55 scanning electron microscope. UV-visible spectra were recorded using a UV-6300PC VWR UV-visible spectrometer. Steady-state photoluminescence (PL) spectra and time-resolved PL (TRPL) data were measured using an Edinburgh Instruments FLS980 spectrometer. The data were obtained using glass/ITO/TiO_2/perovskite. The beam was incident on the film surface and an excitation wavelength of 400 nm was used to obtain the steady-state PL spectra. An excitation wavelength of 405 nm was used to obtain the TRPL data. A Malvern PANalytical XRD 5 was used to obtain XRD diffraction data. A Newport QuantX-300 instrument was used for measuring external quantum efficiency (EQE) data. X-ray photoelectron spectroscopy (XPS) was conducted on an ESCA2SR spectrometer (Scienta Omicron GmbH) using monochromatic Al Kα radiation (1486.6 eV, 25 mA emission at 300 W, 1 mm spot size) at a base vacuum pressure of ~1×10^{-9} mbar. Fourier transform infrared (FTIR) transmission spectra were measured by Bruker ALPHA FTIR spectrometer. Contact angle measurements were performed with a drop of water (60 µL) on the film surface using a Kruss DSA100. Atomic force microscopy (AFM) images were obtained utilizing a Bruker Bioscope Catalyst AFM equipped with a Nanoscope V controller (Bruker UK Ltd, Coventry,

UK). This system operated under the Bruker Nanoscope controller software (v9.15) and mounted on a Nikon Eclipse Ti–I optical microscope (Nikon Instruments Europe B.V.). The image capture process was conducted in air utilising ScanAsyst™ (peak-force tapping) mode with ScanAsyst Air probes. The Bruker Nanoscope Analysis (v1.4) software package (Bruker Corporation, USA) was utilized to analyse the acquired images. Energy-dispersive X-ray (EDX) analysis was performed using a Zeiss Merlin FEG-SEM.

Microsecond transient absorption spectroscopy (TAS) measurements were conducted on thin films of the following architecture ITO/TiO_2/perovskite layer with and without (control) NG-100/Spiro-OMeTAD. The films were sealed under nitrogen in quartz cuvettes (Starna Scientific Ltd., path length 22 mm). A layer of TiO_2 was required to ensure efficient electron extraction from the perovskite layer, and interfacial dynamics of holes in Spiro were spectroscopically observed. Perovskite layers were selectively excited at 510 nm under different excitation fluences using a Nd:YAG laser (OPOTEK, Opolette 355 II, 7 ns pulse width, 9.4 Hz repetition rate) equipped with an optical parametric oscillator to generate 510 nm pulses from the fundamental 1064 nm emission. The excitation power was measured with a power meter (Ophir Vega) and attenuated using neutral density filters. A near-infrared probe at 1600 nm was obtained from a 100 W Quartz Tungsten Halogen lamp (Bentham IL1) using a monochromator and a long pass filter, and focused onto an InGaAs photodiode (Hamamatsu G6849). Sample transmission signal was amplified (Costronics 2004), recorded simultaneously with a Tektronics DPO-2012B digital phosphor oscilloscope (1 μs-10 ms) and a NI-USB-6211 National Instrument DAQ card (0.1 – 100 ms time range) and merged using in-house LabVIEW software.

Centrifugation (14,500 rpm, 2 h) was employed to obtain the nanogel pellets for the moisture trapping test and the humidity was measured using a Multicomp Pro Temperature & Humidity Meter.

Device measurements

The current density - voltage (*J* - *V*) characteristics were measured using a Keithley 2420 Sourcemeter and 100 mW cm^{-2} illumination (AM 1.5G) and a calibrated NREL certified Oriel Si-reference cell. Spectral correction has been applied by using a Newport 91150 V calibrated reference cell. The active area of the devices (0.079 cm^2) was determined using a square aperture within a mask. The data shown are from the reverse scan (V_{oc} to J_{sc}) and the sweep rate was 100 mV s^{-1}. The data measured using the reverse sweep are reported unless otherwise stated. A Keithley 2420 source meter was also used for measuring the SCLC characteristics of electron only devices. The light soaking tests were performed under full AM 1.5 sun-equivalent using white-light LED arrays. *Non*-encapsulated devices were used *without* any UV-protection. These measurements were conducted in ambient air and the devices were heated to 30 °C during the irradiation. Applied cooling was *not* applied. The relative humidity during these experiments was 35% ± 10%. Periodically, each device was briefly removed to conduct *J-V* measurements (as described above) and then immediately returned.

Adhesive tape test

Adhesive tape tests were conducted by using a double-blind experiment protocol. The four samples were randomly placed in a plastic dish and the corresponding identity of the films was recorded on a notebook. Two testers then chose two samples for the test. Lines were scribed onto the glass/ITO/bl-TiO_2/perovskite-nanogel surface in vertical and horizontal directions. A rubber roller was used to apply uniform pressure to the tape (Eurocel). The tape was applied horizontally for 120 s and vertically for 60 s, then repeated the same process once. After that, the tape was removed rapidly in a perpendicular direction to the film surface. After all experiments were finished, the samples were put back into the plastic dish in order, and the identity of the samples were revealed. During the whole process, the identity of the samples was not known to the testers. The proportion of the film detached was measured using ImageJ.

Computational methods

Our *ab-initio* calculations were performed using a plane-wave/pseudopotential DFT approach as implemented in the Vienna Ab-initio Simulation Package (VASP)[1-3]. The generalized gradient approximation (GGA) exchange-correlation functionals of Perdew Burke-Ernzerhof modified for solids (PBEsol)[4] was used. The Gimme's DFT-D3 dispersion correction term[5] was added to all of our total energy calculations. The planewave-type basis sets with a kinetic energy cut-off of 500 eV and a gaussian smearing of 0.01 were implemented for the self-consistent field (SCF) method calculations, with a convergence criterion of $1x10^{-6}$ eV. For geometry optimizations, a k-point grid of 4x4x4 was used for bulk system (2x2x1 for surface slab). For electronic structure calculations, a finer 6x6x6 k-point grid was used for bulk system (4x4x1 for surface slabs). Such DFT methods have been applied to previous studies of perovskite halides successfully[6-8].

Using the DFT-optimized monomer-surface structure as the initial configuration, our *ab-initio* molecular dynamics (AIMD) calculations were performed at 300 K for a total duration of 10 ps in the NVT ensemble. To accurately describe the C-H and N-H vibrations, a time step of 1 fs was taken. To reduce the computational load at each step, a reduced kinetic energy cut-off of 300 eV and a gaussian smearing of 0.1 were implemented for the electronic calculations. In our analysis, only the results after the 3rd picosecond, when the MD instantaneous temperature was stabilized, were considered.

Our PbI_2-terminated (001) surface slab was constructed by taking the structure of the fully optimized 2x2x2 α-$FAPbI_3$ supercell. A 4x4x3 slab structure was constructed with a vacuum region of 20 Å on top to avoid any spurious interactions between the periodic images. The bottom sheet of Pb/I atoms were removed to keep the slab stoichiometric vertically. During the geometry optimizing calculations, the bottom layer was fixed for two reasons: maintaining the bulk lattice parameters and reducing the computational expense. For the selection of the most favourable monomer, 10 different conformations of MEO_2MA monomers (obtained from the online database[9]) were optimized in a

28x28x28 $Å^3$ cubic vacuum box. The lowest-energy monomer was then placed over the centre of and parallel to the perovskite surface as the starting configuration of geometry relaxation. After the structures were optimized, the binding energies were calculated as: $E_{Binding} = E_{Tot}^{S+M} - E_{Tot}^{S} - E_{Tot}^{M}$, where E_{Tot}^{S+M}, E_{Tot}^{S}, and E_{Tot}^{M} are the total energies of surface-monomer, surface-only, and monomer-only in the same simulation box respectively.

Method for the simulations of MEO_2MA-PbI_2

The DFT simulations of MEO_2MA-PbI_2 interactions were carried out using the NWChem code[10]. To accurately describe the molecular binding interactions, the double-hybrid range-separated exchange-correlation functional ωb97x with the Gimme's DFT-D3 empirical dispersion correction[5, 11] were employed. After the structures were optimized, the binding energies were calculated as: $E_{binding}^{M+PbI2} = E_{Tot}^{M+PbI2} - E_{Tot}^{PbI2} - E_{Tot}^{M}$, where E_{Tot}^{M+PbI2}, E_{Tot}^{PbI2}, and E_{Tot}^{M} are the total DFT energies of monomer-PbI_2, PbI_2-only, and monomer-only respectively.

SUPPORTING DATA

VIDEO

Video S1. The association of MEO_2MA monomer and the pristine perovskite surface at 300 K.

Video S2. The association of MEO_2MA monomer and the defective perovskite surface at 300 K.

FIGURES

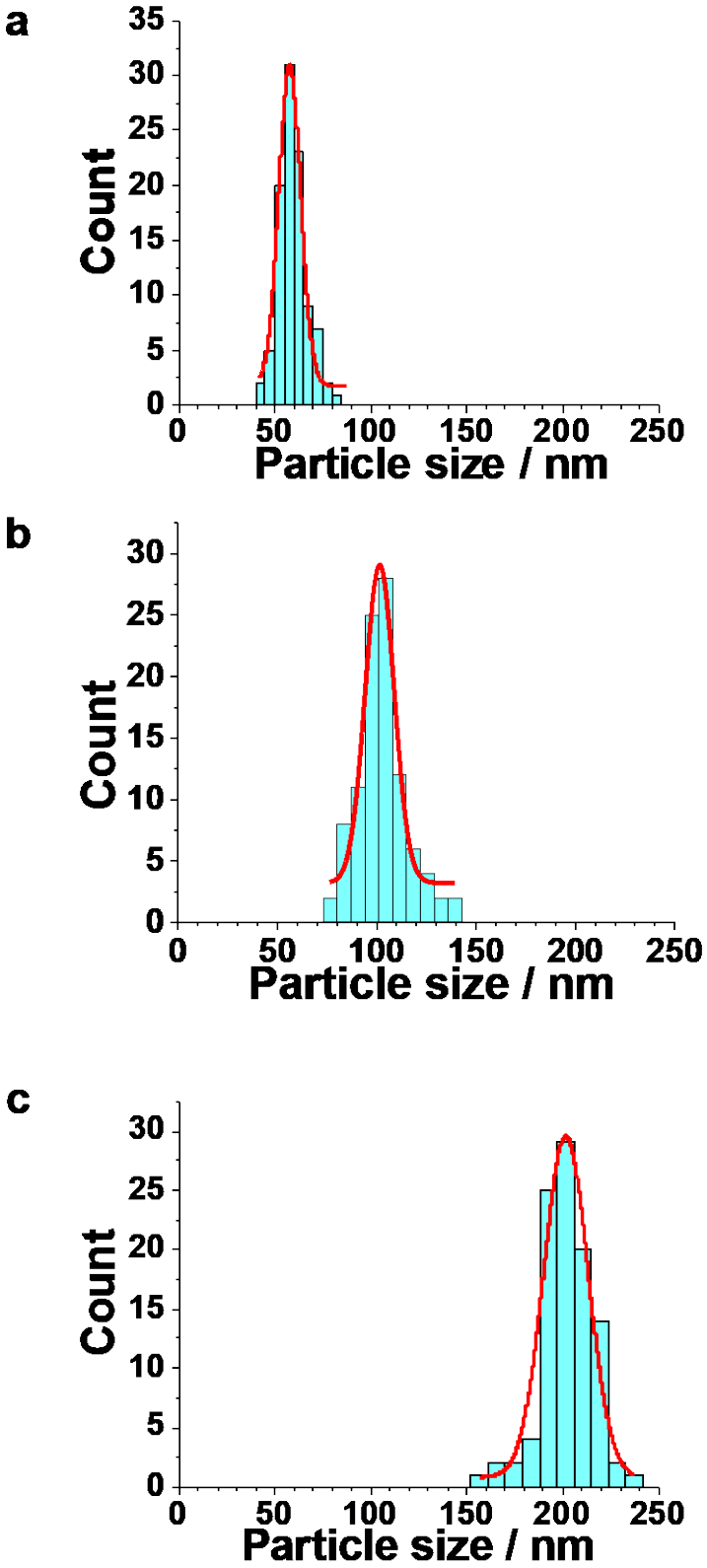

Fig. S1. Particle size distribution from SEM data for **(a)** NG-60, **(b)** NG-100 and **(c)** NG-200.

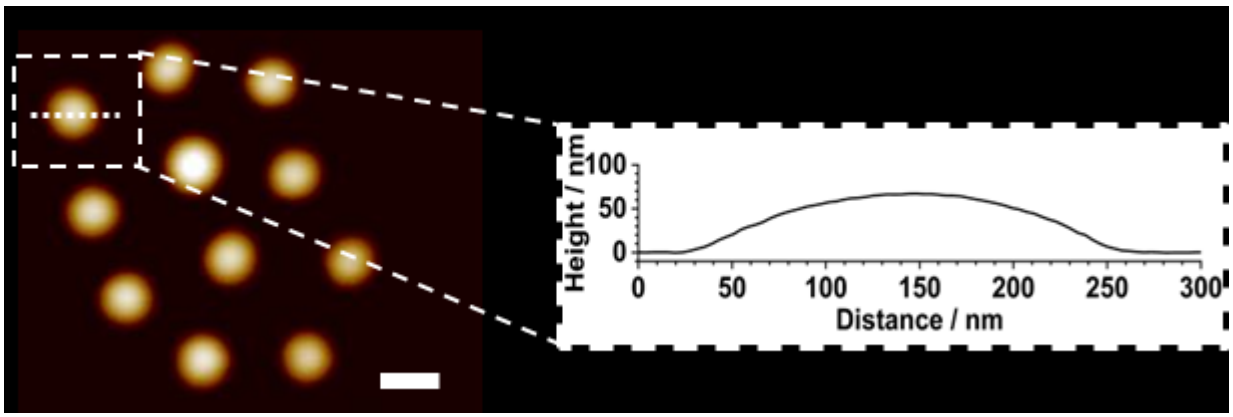

Fig. S2. AFM image for NG-200 and line profile for a representative particle. The line profile was measured from the dashed line. Scale bar = 200 nm.

Note 1: Additional discussion regarding swelling of the hydrophilic nanogels

$PMEO_2MA$ nanogels (Fig. 1a) have temperature-responsive properties in water[12]. DLS data (Fig. S3a) show that the nanogels are swollen and hence, hydrophilic, in water at 20 °C. However, they deswelled at higher temperature in water and were fully collapsed at 60 °C. This is due to the temperature triggered disruption of hydrogen bonding between water and the ether oxygens[12]. We use the z-average (d_z) diameters at 60 °C in water as a measure of the collapsed spherical size of the nanogels. These values are 33, 53 and 160 nm, respectively, for NG-60, NG-100 and NG-200 (Table S2). Using these values it can be shown that for every one NG-200 particle there would be approximately 100 NG-60 particles and 30 NG-100 particles at the same total nanogel concentration.

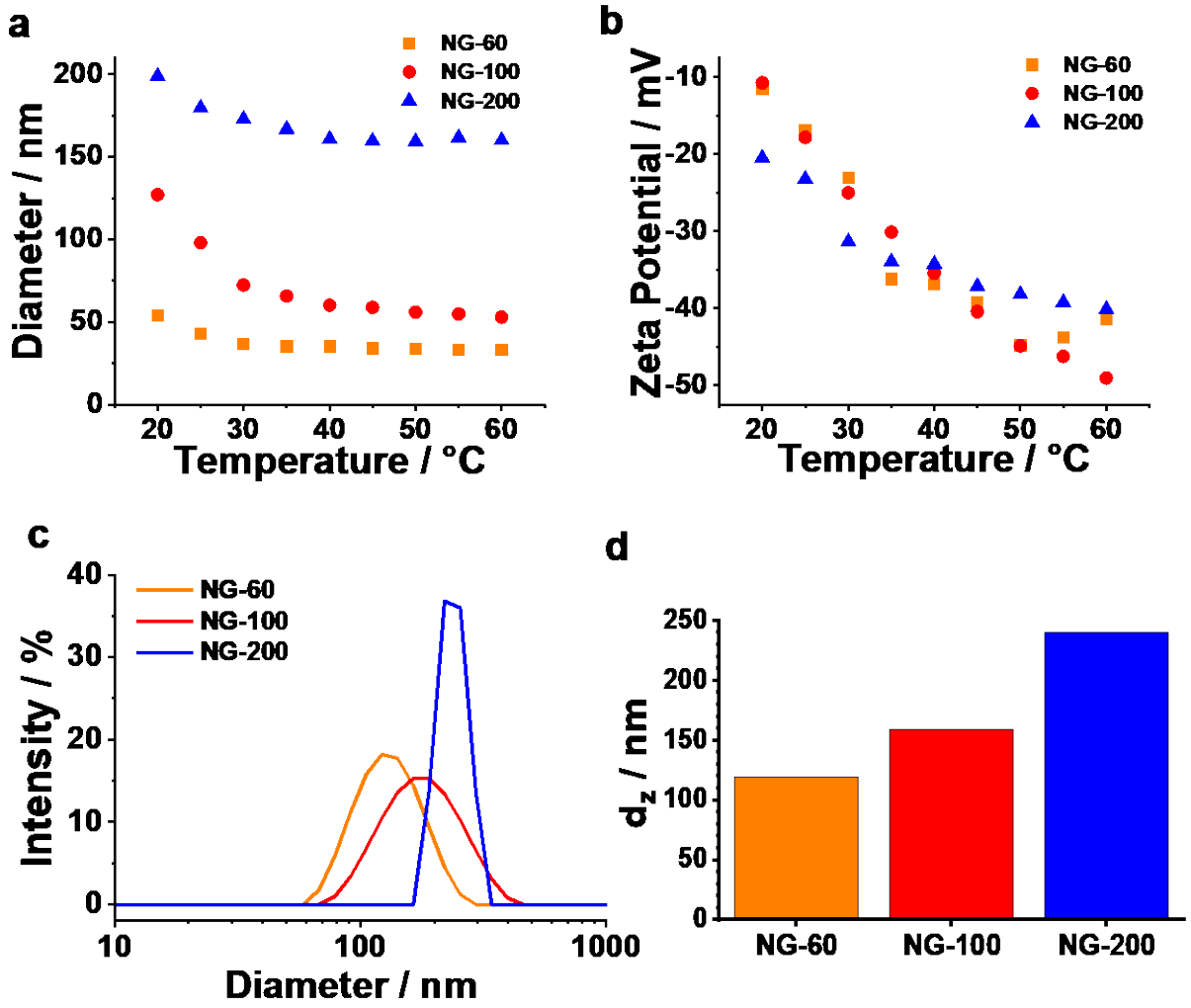

Fig. S3. (a) Temperature-dependent z-average diameters (d_z) and **(b)** zeta potential values for NG-60, NG-100 and NG-200 particles dispersed in water. **(c)** DLS diameter distributions for the nanogels dispersed in DMF at 50 °C. **(d)** Z-average diameters obtained from the distributions shown in (c).

Zeta potential data were also measured (Fig. S3b) and show the nanogels are negatively charged. The zeta potential becomes more negative at higher temperature because the particles collapse in water when heated (see above). The charge present originates from the persulfate initiator used during their synthesis.

Although the $PMEO_2MA$ nanogels de-swell and collapse in water as the temperature increases they show the opposite behavior in non-aqueous solvents[13]. We find that these nanogels swell in DMF when the temperature is *increased* from room temperature to 50 °C. The diameter distributions and d_z values are shown in Fig. S3c and S3d, respectively. The d_z values for NG-60, NG-100 and NG-200

are 119, 159 and 240 nm, respectively. We used heating of the nanogels in DMF at 50 °C to improve dispersion of the nanogels in the perovskite precursor solution prior to film formation.

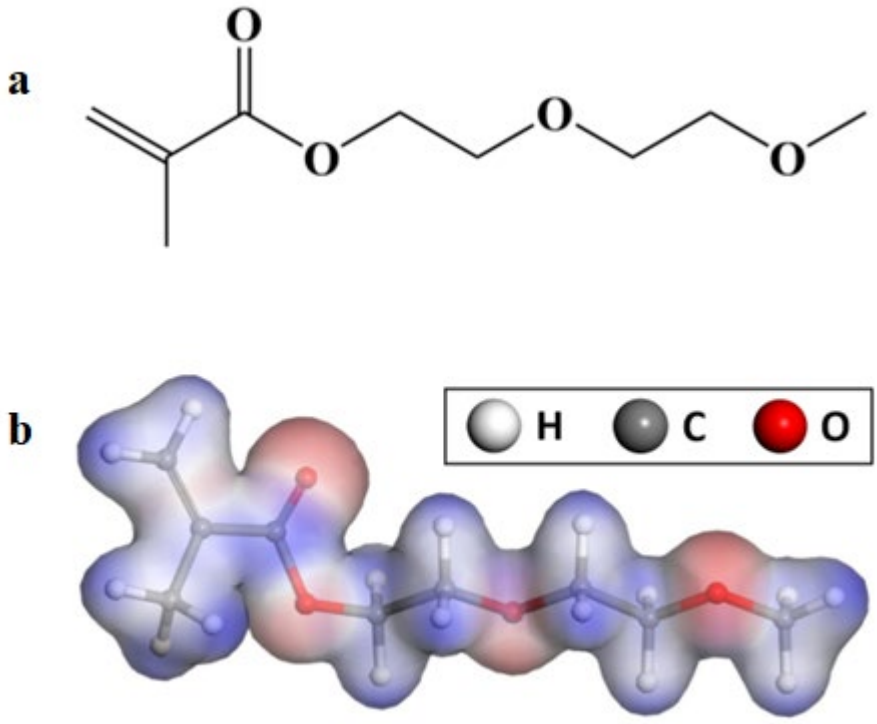

Fig. S4. (a) Schematic representation of MEO_2MA monomer and **(b)** ball-and-stick diagram of the most stable conformation of MEO_2MA and its charge density isosurface colored with respect to electrostatic potential.

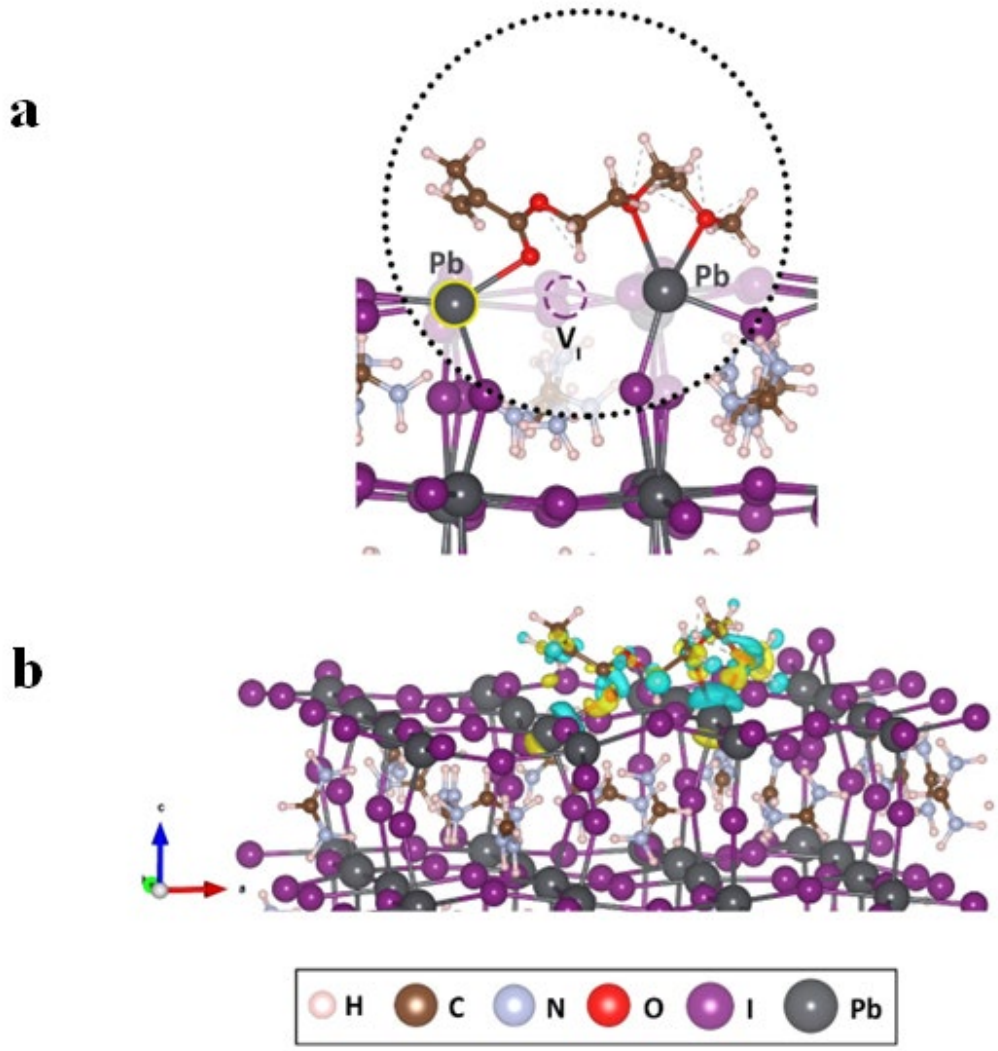

Fig. S5. Side view of the other stable configuration **(a)** and charge transfer density difference **(b)** of MEO_2MA bonding with the other Pb ion adjacent to the I vacancy (V_I) site on the (001) PbI_2-terminated $FAPbI_3$ surface. The binding energy calculated from this configuration is 0.26 eV higher than the counterpart reported in the main text.

Note 2: Preliminary study identifying the optimum nanogel concentration for device efficiency

An initial study was conducted into the effect of NG-100 concentration on the device performance and the data are shown in Fig. S6 and Table S4. The addition of 3.0 mg/g of NG-100 increased the V_{oc}, FF and PCE values. The best PCE values for the 0 (control), 3.0 and 10 mg/g devices are 18.40%, 20.08% and 18.73%, respectively. These PCE differences are dominated by V_{oc} and FF.

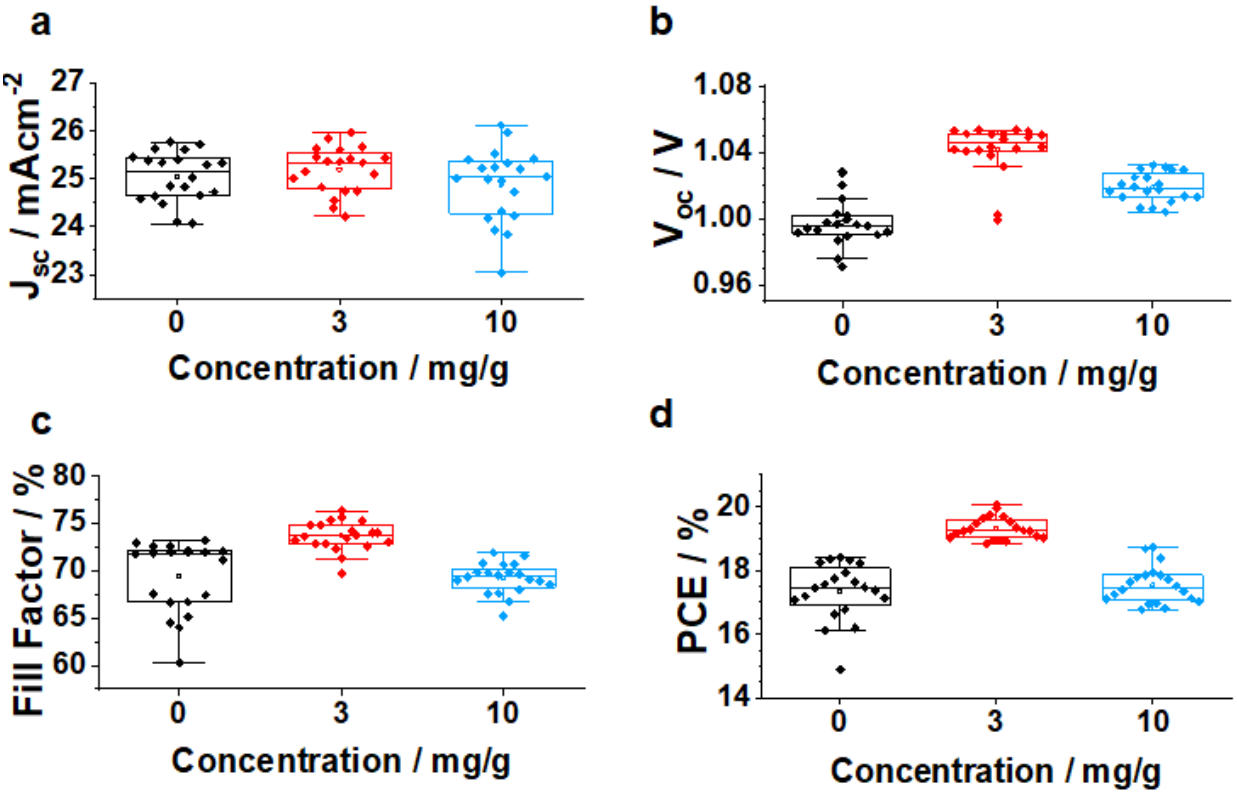

Fig. S6. Measured **(a)** short-circuit current densities, **(b)** open-circuit voltages, **(c)** fill factors and **(d)** PCEs for NG-100 and control devices. The x-axis shows the NG-100 concentration.

We attribute the decrease in the PCE value at 10 mg/g to an increase of the concentration of insulating NG-100s at the surface of the perovskite grains as well as decreased film quality (Fig. S9). Support for the former suggestion comes from water contact angle measurements performed at a range of NG-100 concentrations (Fig. S7). The contact angle decreases as the concentration of hydrophilic nanogel particles increases at the surface. Accordingly, we used a nanogel concentration of 3.0 mg/g to study the effect of nanogel size on PSC performance in this study.

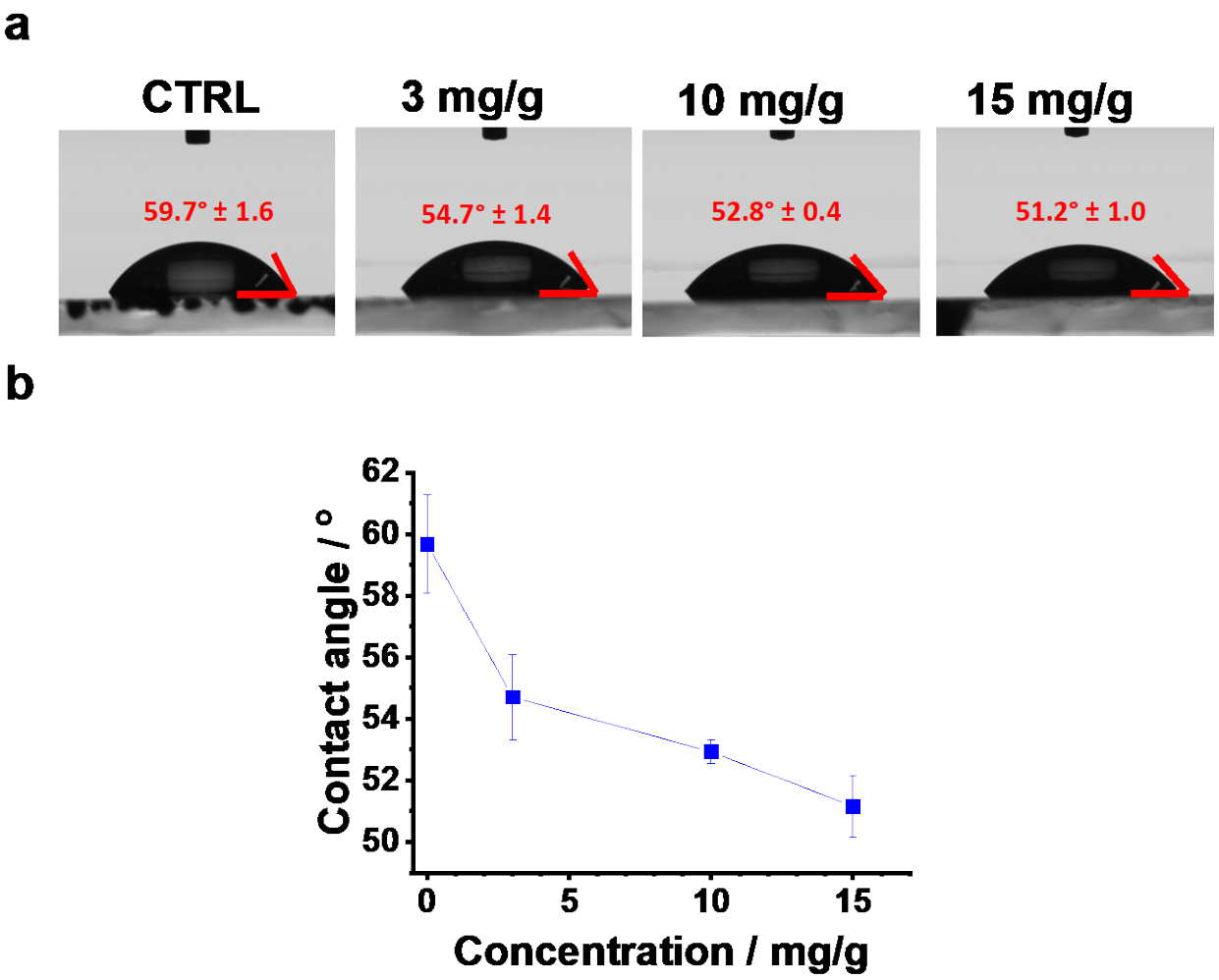

Fig. S7. (a) Photographs showing water droplets on perovskite films prepared using a range of NG-100 concentrations. **(b)** Contact angle values obtained from (a) for the various perovskite/NG-100 systems.

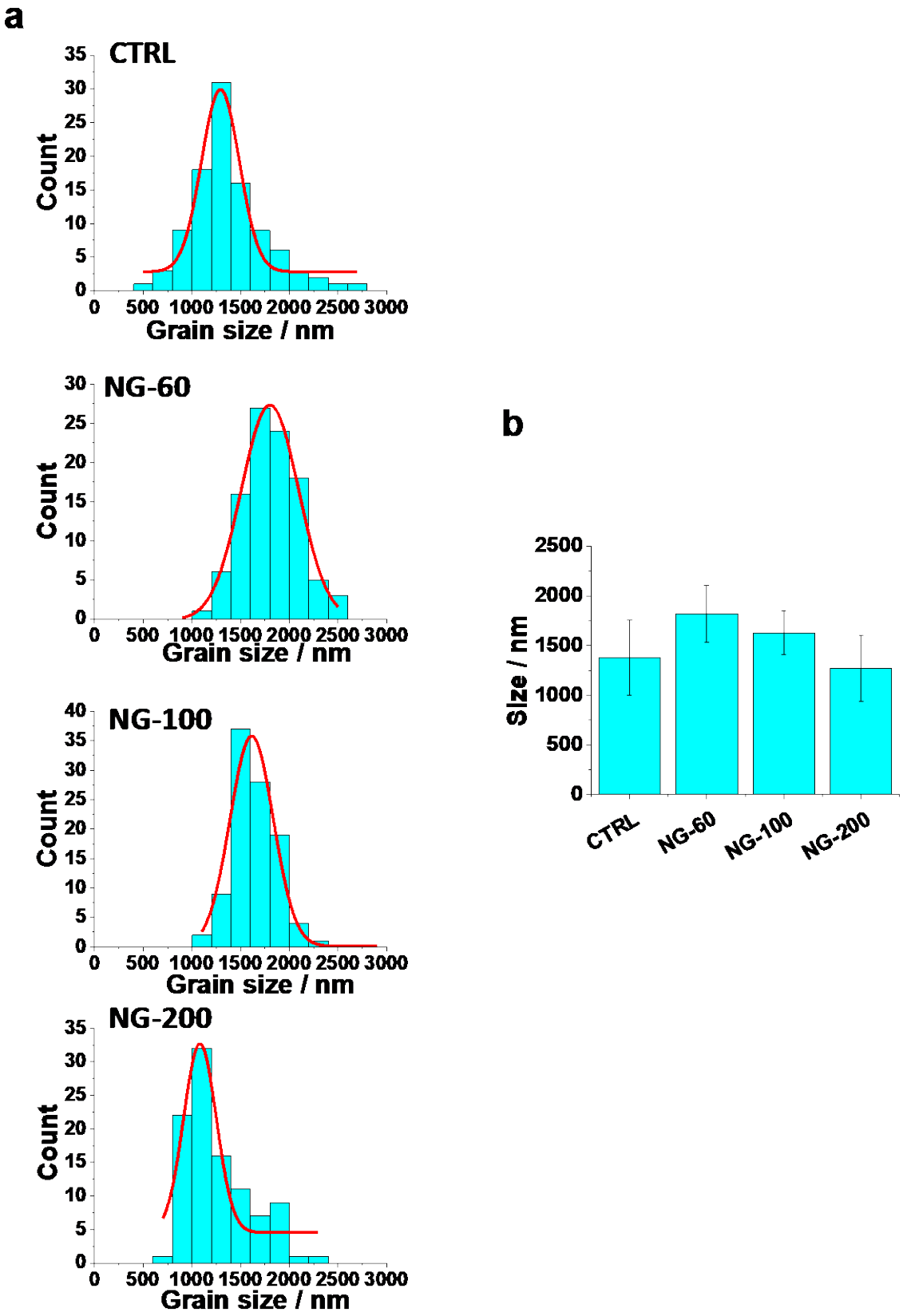

Fig. S8. (a) Grain size distributions of perovskite films prepared using different nanogels and **(b)** average grain sizes from (a).

Note 3: Estimating the specific surface area of the nanogel particles

The specific surface area (A_s) of nanogels with a collapsed diameter of d_{Coll}, can be calculated from the ratio of the particle surface area to the mass of the particle. Treating the collapsed nanogels as spheres, the following equation can be shown.

$$A_S = \frac{6}{\rho d_{Coll}} \qquad \text{(S1)}$$

where ρ is the density of the polymer, which is taken as 1.1 x 10^6 g.m^{-3}. For d_{coll} we use the d_z values for the nanogels in water at 60 °C (Table S2). Accordingly, the calculated A_s values for the NG-60, NG-100 and NG-200 particles are 165, 103 and 34 m^2.g^{-1}. A value of 165 m^2.g^{-1} implies that 1.0 g of NG-60 particles could, in principle, cover a surface having an area of 165 m^2.

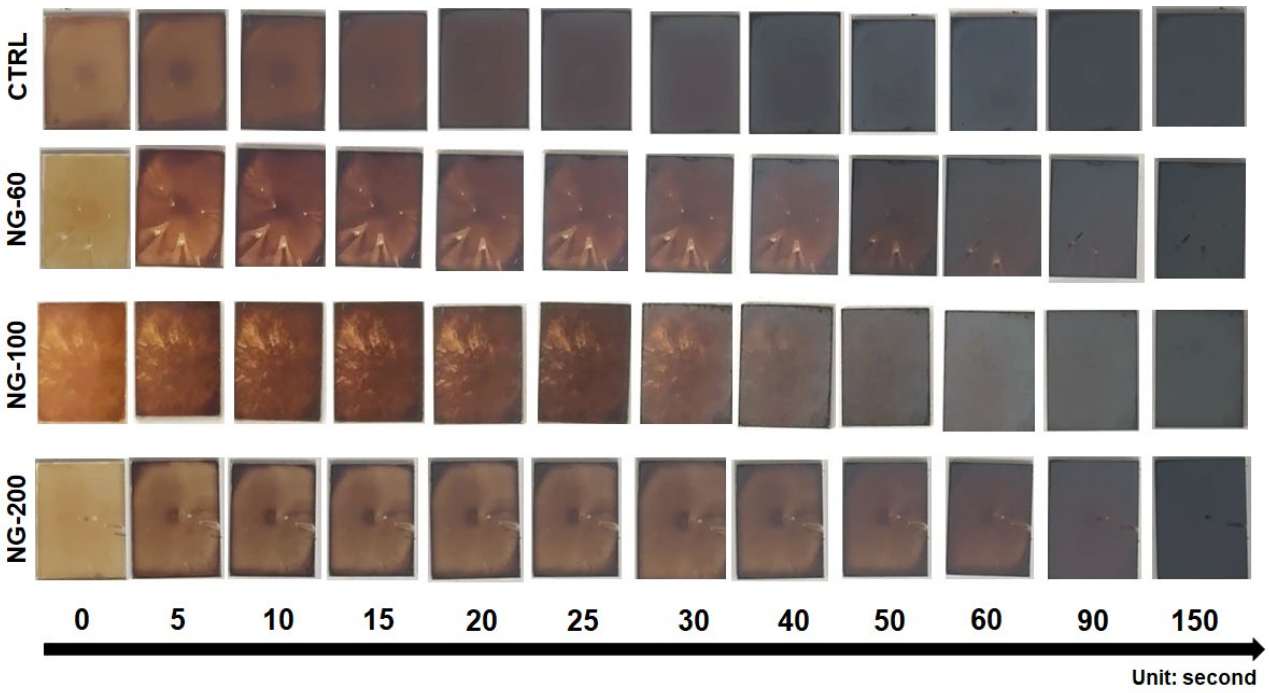

Fig. S9. Digital photographs of various perovskite films as a function of time (shown in seconds) whilst annealing at 50 °C with or without addition of various nanogels (10 mg/g). Film dimensions: 20 mm x 15 mm.

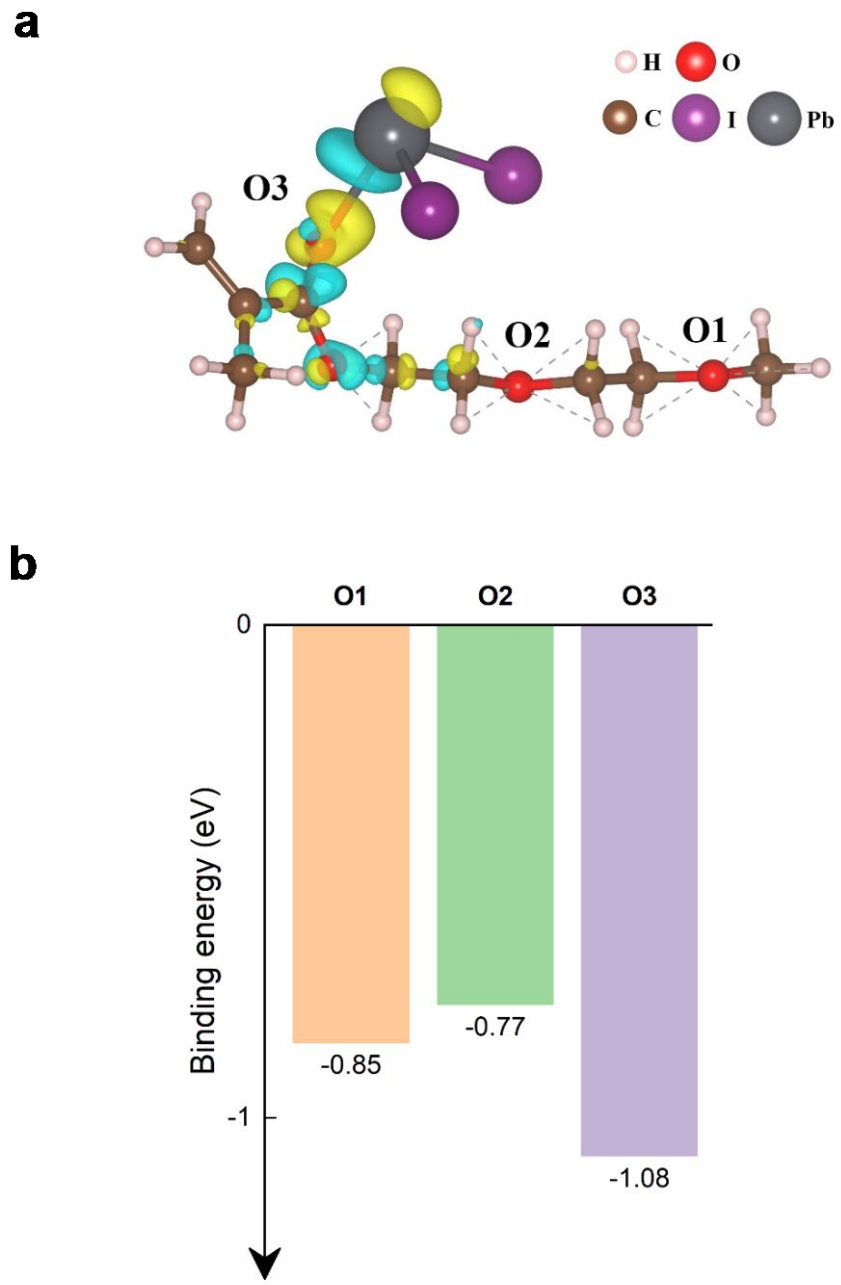

Fig. S10. (a) Ball-and-stick diagram of the optimized configuration and charge transfer density of an MEO_2MA monomer binding with a PbI_2 molecule. **(b)** The binding energies of PbI_2 molecule binding with different oxygen atoms on the MEO_2MA monomer.

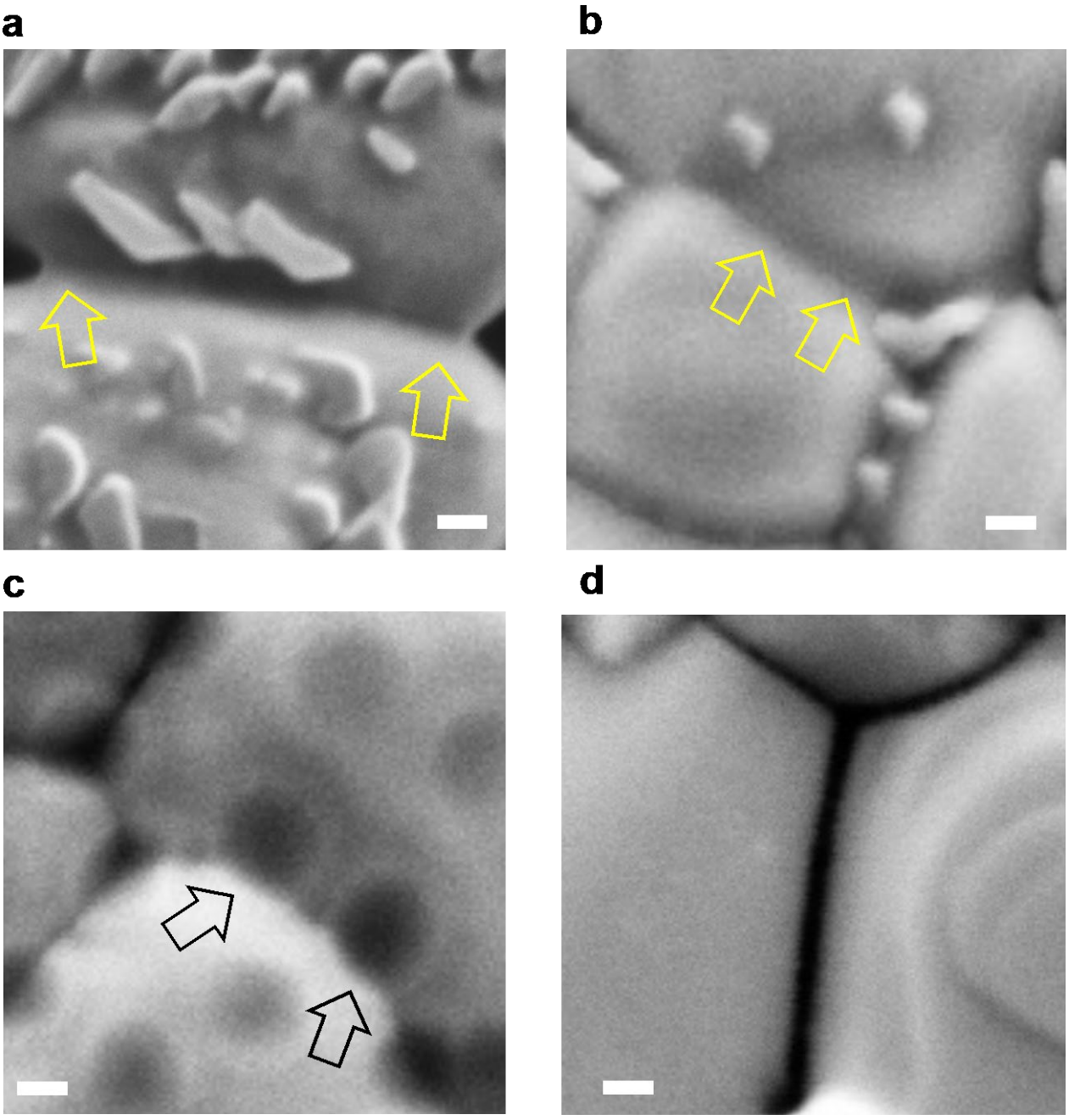

Fig. S11. Higher magnification top view SEM images from Fig. 3 of the perovskite films prepared using **(a)** NG-60, **(b)** NG-100, **(c)** NG-200 and **(d)** the control without nanogels. The yellow arrows highlight nanofilm bridges between perovskite grains. The black arrows in (C) show where individual NG-200 particles bridged two perovskite grains. Scale bars: 100 nm.

Note 4: Relationship between vertical perovskite nanocrystals and nanogel coverage

We noticed that vertical nanocrystals were present on the surfaces of the grains for some of the nanogel systems (Fig. 3) and investigated this unusual observation in more detail. Firstly, we increased the NG-200 particles concentration to 10 mg/g and examined the perovskite/NG-200 film using SEM (Fig. S12a). Many vertical nanocrystals are evident and they appear to be mostly closely associated with the NG-200 particles. Either the nanocrystals grew near one edge of a NG-200 particle or they grew on top of a NG-200 particle. To further examine this phenomenon we obtained AFM data for this system (Fig. S12b). NG-200/nanocrystal pairs are evident. A representative line profile of an isolated NG-200 particle shows that it flattened on top the perovskite grain (Fig. S12c) with a particle diameter and height of 234 and 44 nm, respectively. This flattening which is intrinsic to deformable nanogels brings additional (previously hidden) polymer functional groups (in this case C-O groups) into direct contact with the perovskite and thereby increases passivation. Furthermore, a line profile for a NG-200/nanocrystal pair (Fig. S12d) shows that the nanocrystal sits against part of the NG-200 particle. Hence, these SEM and AFM data indicate that vertical nanocrystals are associated with nanogels.

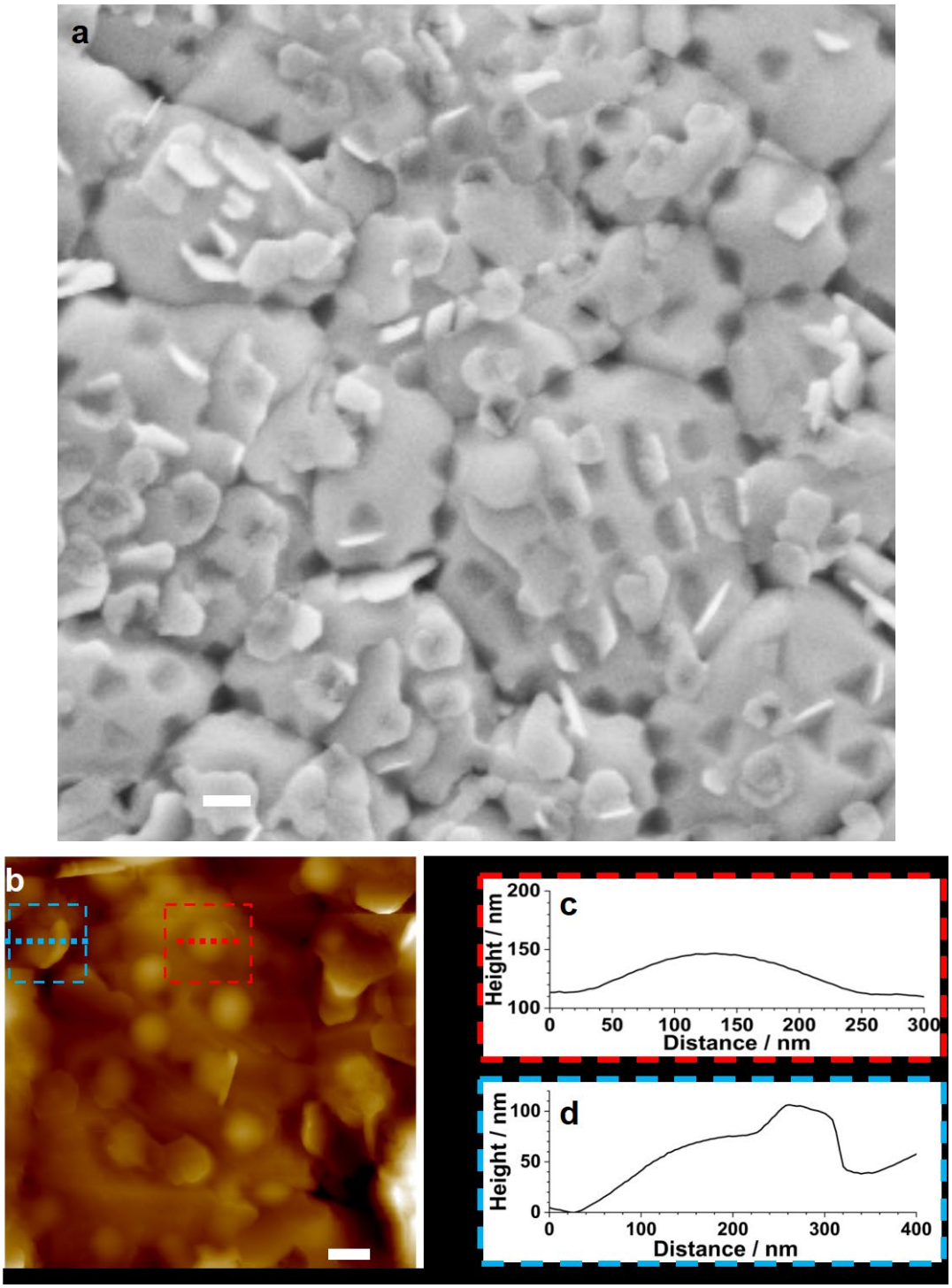

Fig. S12 (a) Representative SEM image of a perovskite/NG-200 film prepared using a nanogel concentration of 10 mg/g. **(b)** Height mode AFM image for a representative NG-200 particle on top of a perovskite grain (10 mg/g). **(c)** and **(d)** show line profiles, respectively, for an isolated NG-200 particle and a NG-200 particle/nanocrystal pair obtained from (b). The dashed lines show where the line profiles were measured. Scale bars: 200 nm.

There could be a number of potential reasons for this growth mode during crystallization. In general, three-dimensional crystalline materials growth occurs mainly in two dimensions, with ions attaching to step edges or kink sites as these produce the greatest energetic payback in terms of enthalpy. The flux of ions attaching to the growing crystal must be greater than the flux of ions departing the crystal, which leads to this mode of growth. Attachment is energetically favourable at both step edges and kink sites while release is unfavorable, and the equilibrium between ions bound in the crystal and in solution is driven forward. Nanogels act as 'impurities' which affect the kinetics of the growth at step and kink sites in four possible ways.

(1) By step pinning, where the nanogel may bind to the step and block ion flux. The step may continue to grow at the nanoscale, but only if the curvature of the crystalline salients around the nanogel is greater than the critical radius of the hybrid perovskite material i.e., the radius at which the bulk free energy becomes greater than the surface interfacial energy.
(2) From incorporation of nanogels into the growing crystal. This distorts the crystal away from ideal growth habits and could be possible based on the SEM image in Fig. S12a.
(3) From blocking at the kink sites. This overall also lowers the rate of crystallization. However, this is probably not likely in the present case as it often leads to crystallites that have ill-defined cauliflower type surface morphology.
(4) The nanogel acts as a surfactant. The nanogels would physi- or chemisorb to a certain facet with an associated Bragg plane in the growing crystal, lowering the interfacial energy and increasing the rate of growth of the facet (as rate ~ $A\exp(-E_{interfacial}/kT)$). As there is texturing of the crystals in the (100) plane in this case (based on the XRD data in Fig. S25a) it would seem that this mechanism is also quite likely.

Overall, we suggest that (2) and/or (4) are the most likely mechanisms that are responsible for the nanogels causing vertical crystal growth in our systems.

We next explored the effect of NG-100 particle concentration on the morphology of the perovskite/NG-100 films (Fig. S13). Nanofilm formation and grain coverage increase as the NG-100

particle concentration increases. The grain coverage increase by the nanogels is evidenced by the contact angle data (Fig. S7b). Also, the extent of vertical nanocrystal coverage increases as the NG-100 concentration increases. These data confirm that vertical nanocrystal coverage of the grain surfaces is an indirect indicator of nanogel surface concentration.

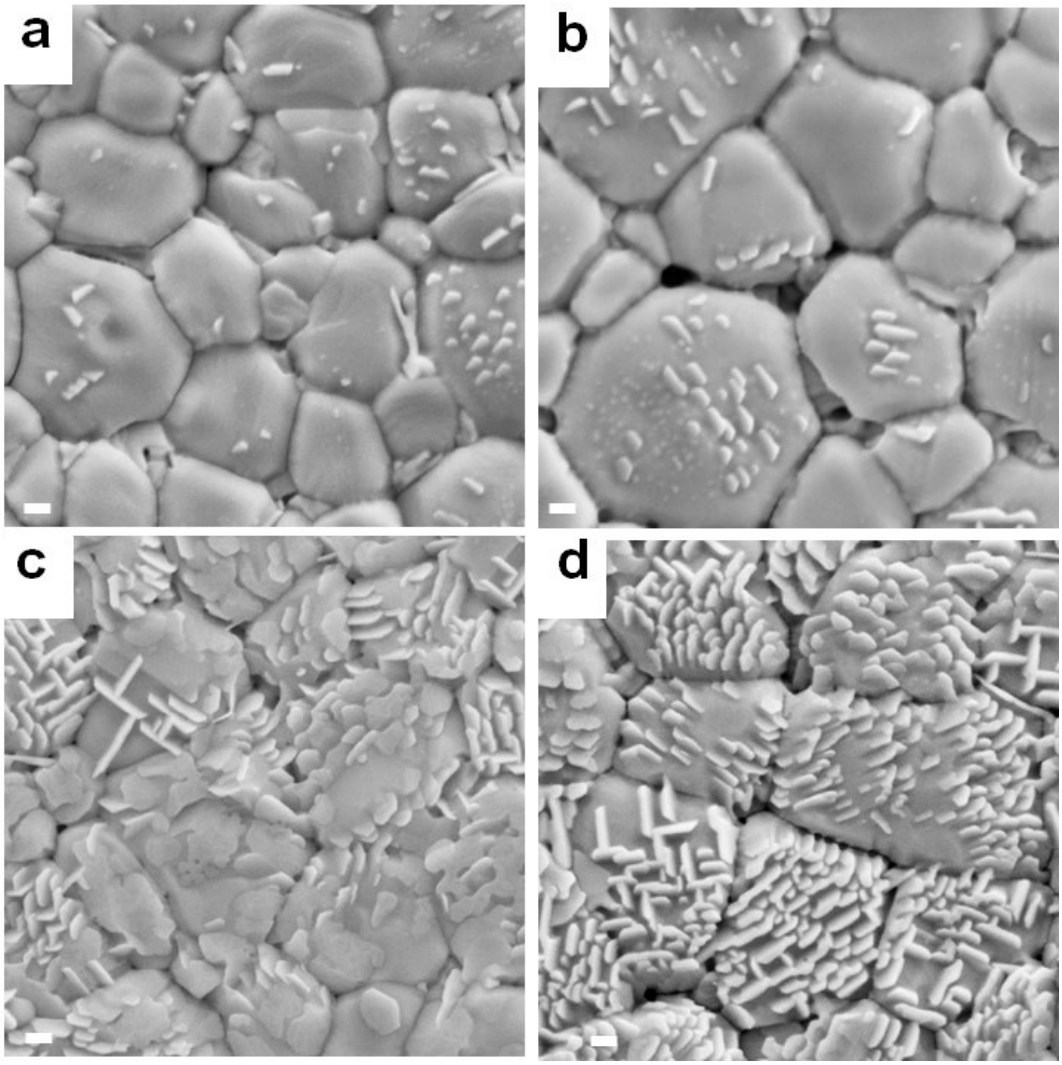

Fig. S13. SEM images for perovskite/NG-100 films prepared using **(a)** 3.0, **(b)** 6.0, **(c)** 10 and **(d)** 15 mg/g NG-100 concentrations. Scale bar = 200 nm.

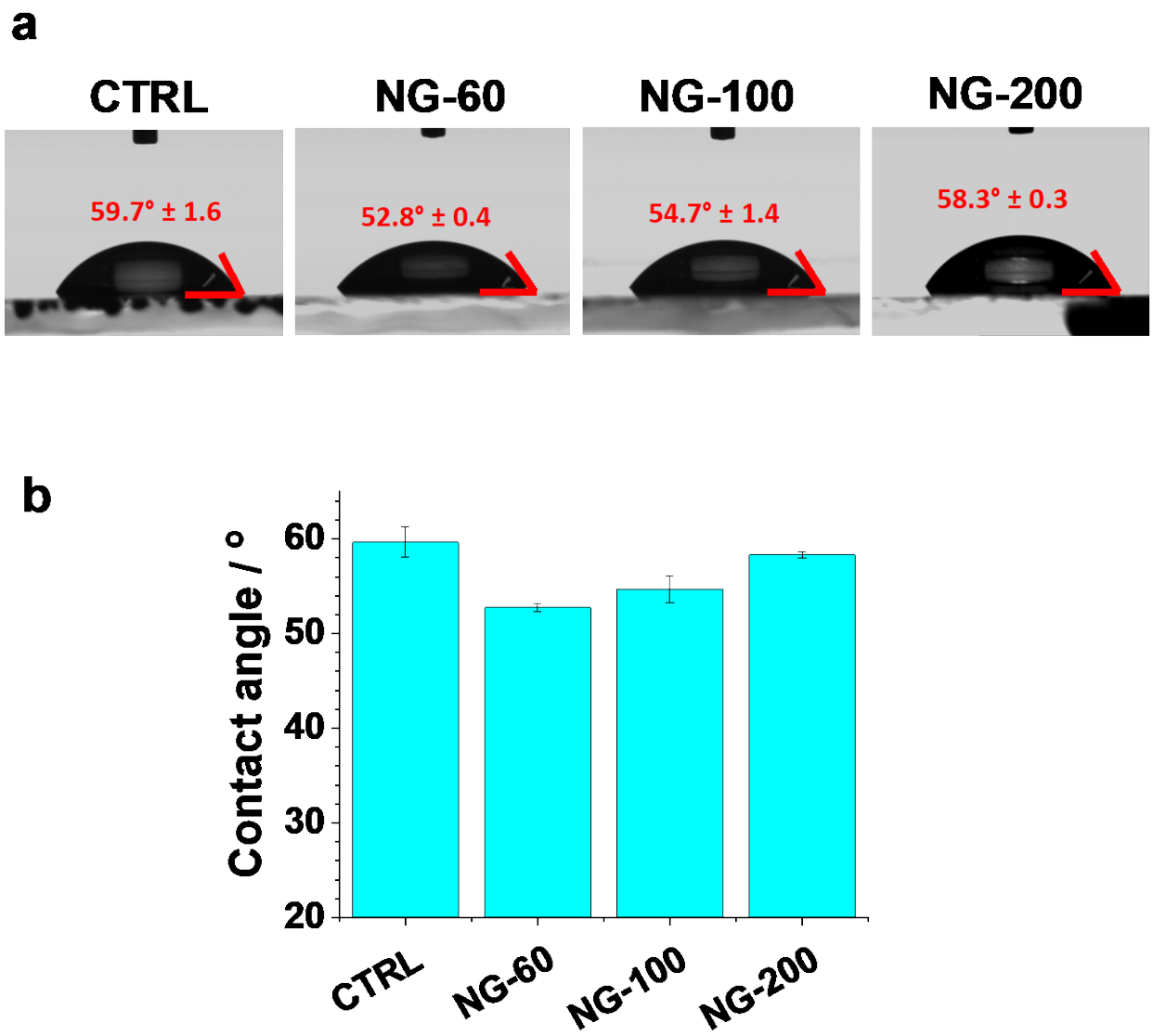

Fig. S14. (a) Photographs showing water droplets on various perovskite films. **(b)** Contact angle values obtained from (a) for the perovskite/nanogel systems.

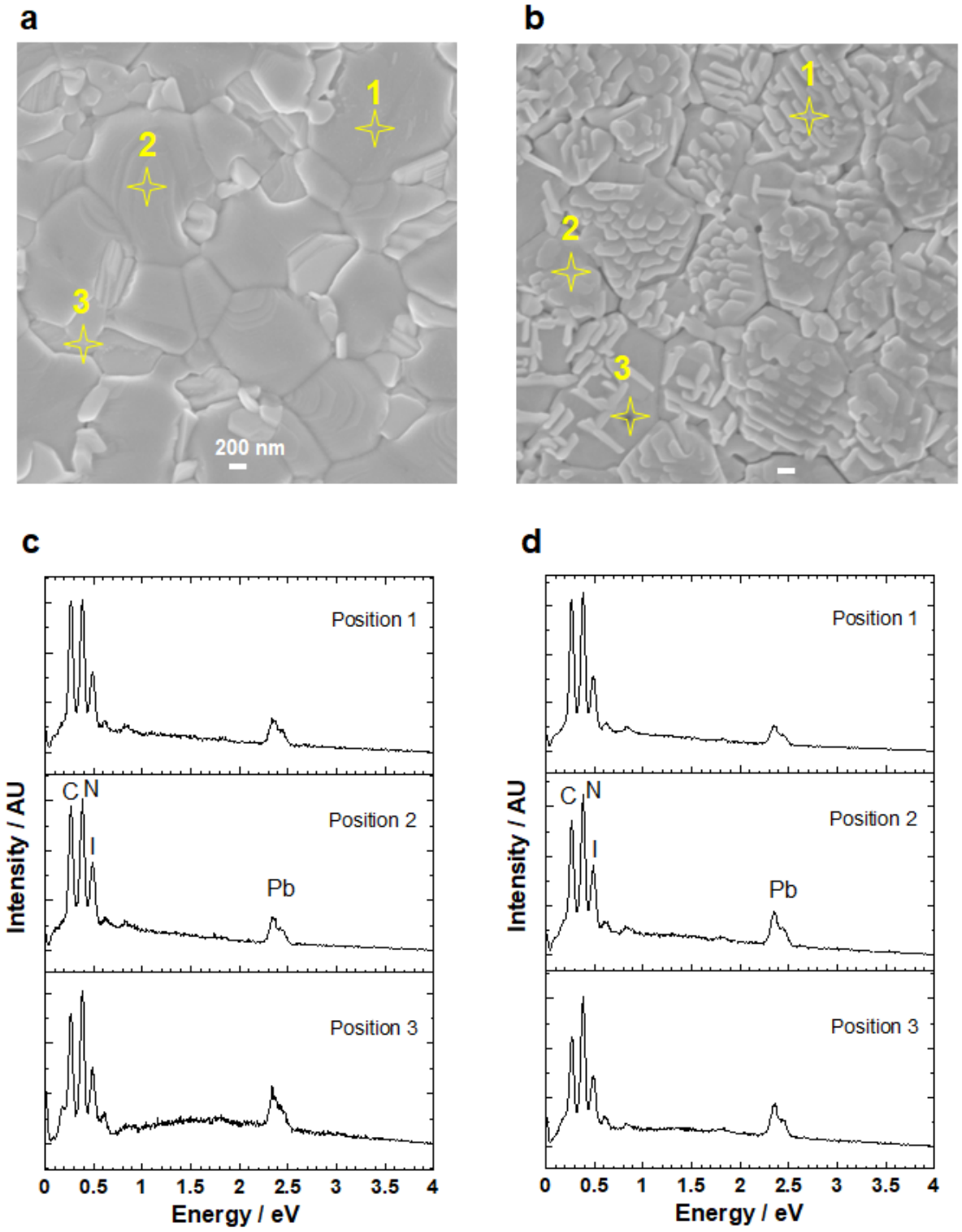

Fig. S15. SEM images for the **(a)** control film and **(b)** perovskite/NG-60 (3 mg/g) film. The yellow crosses and labels show the positions where the EDX spectra were obtained. Position 1 for the NG-60 film targets vertical nanocrystals. The scan spot sizes (62 nm) are smaller than the crosses. EDX spectra obtained from each position for **(c)** the control and **(d)** 3 mg/g NG-60 film are shown. The signal positions for C, N, I and Pb are shown. Data from this investigation appear in Table S5.

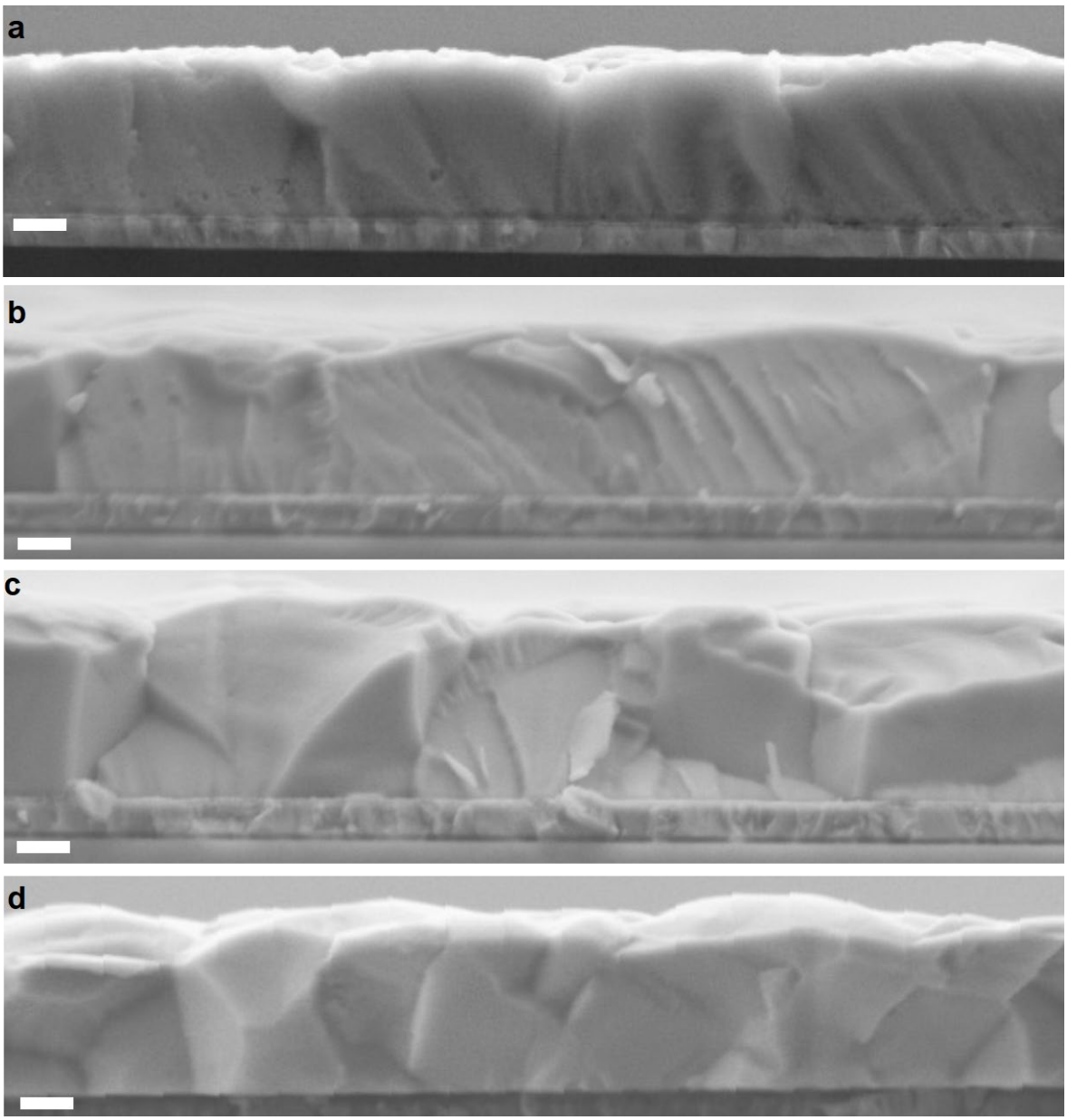

Fig. S16. Representative cross-section SEM images of the perovskites prepared using **(a)** NG-60, **(b)** NG-100, **(c)** NG-200 and **(d)** without added nanogels. Scale bars: 200 nm.

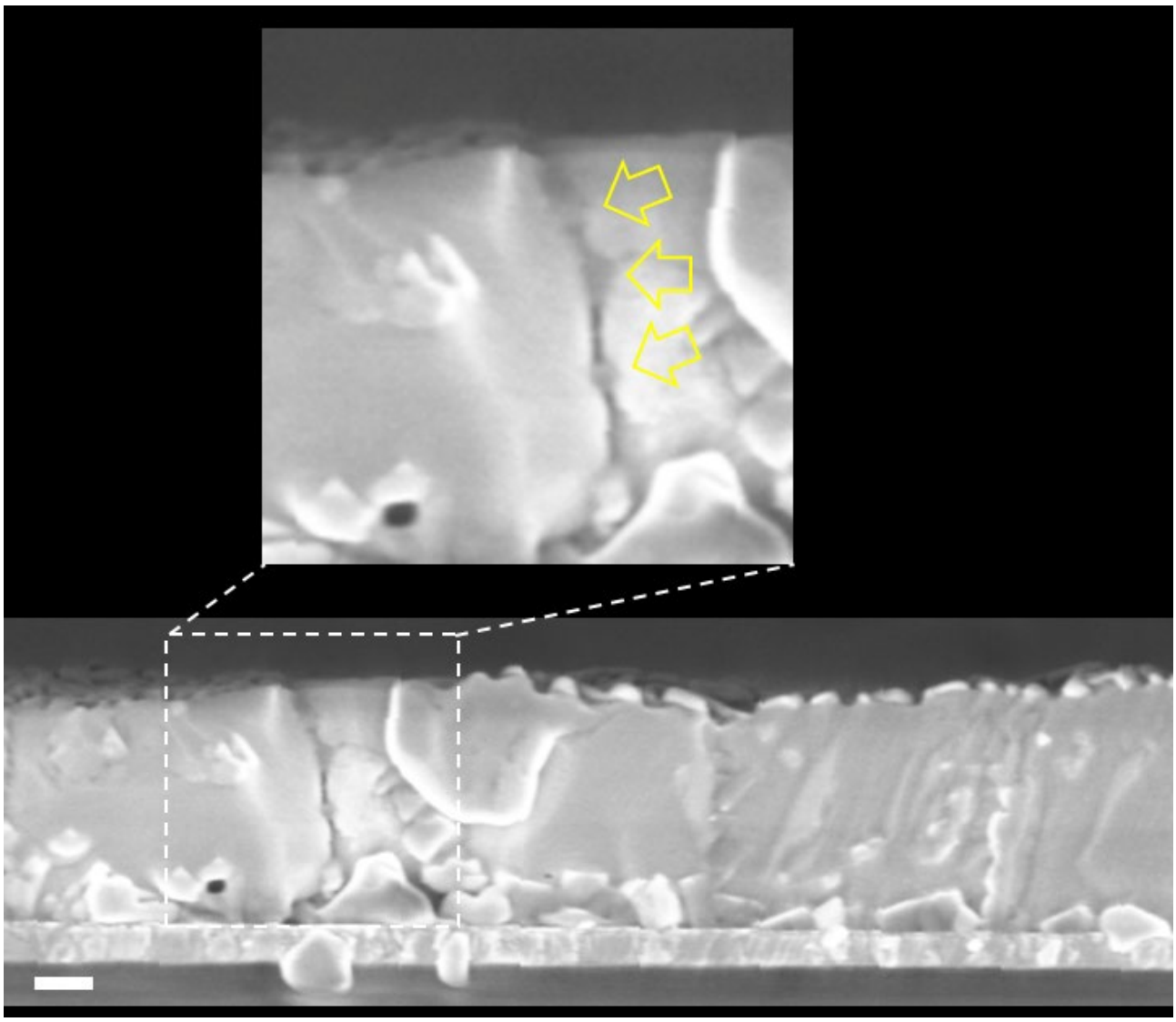

Fig. S17. Representative cross-section SEM image of perovskite/NG-100 prepared using 20 mg/g of NG-100. The inset shows individual and coalesced NG-100 particles between perovskite grains (yellow arrows). The scale bar is 200 nm.

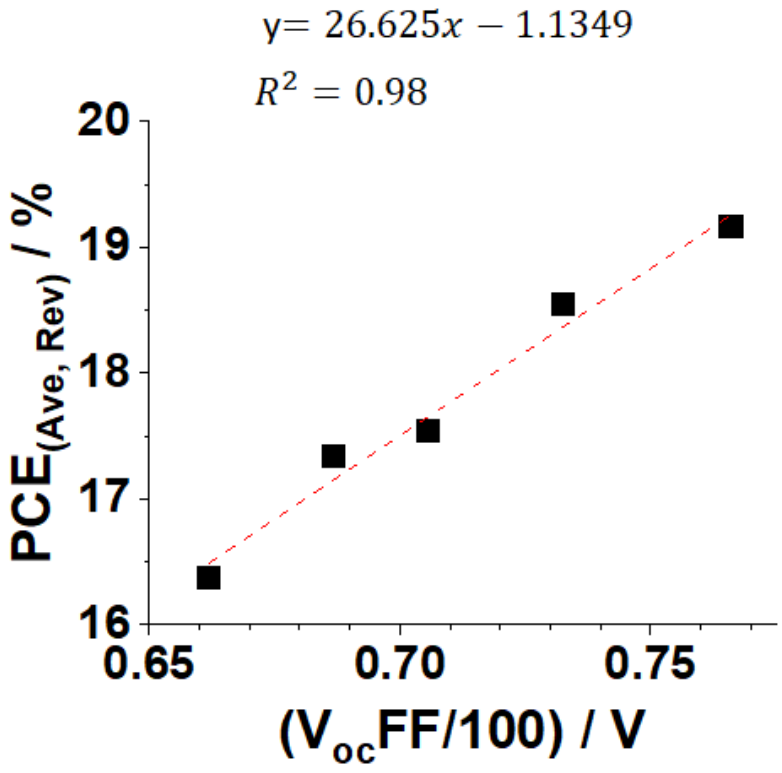

Fig. S18. Variation of the average PCE measured during the reverse sweeps with the product of V_{oc} and (FF/100) for the devices. The equation used to fit the data is shown.

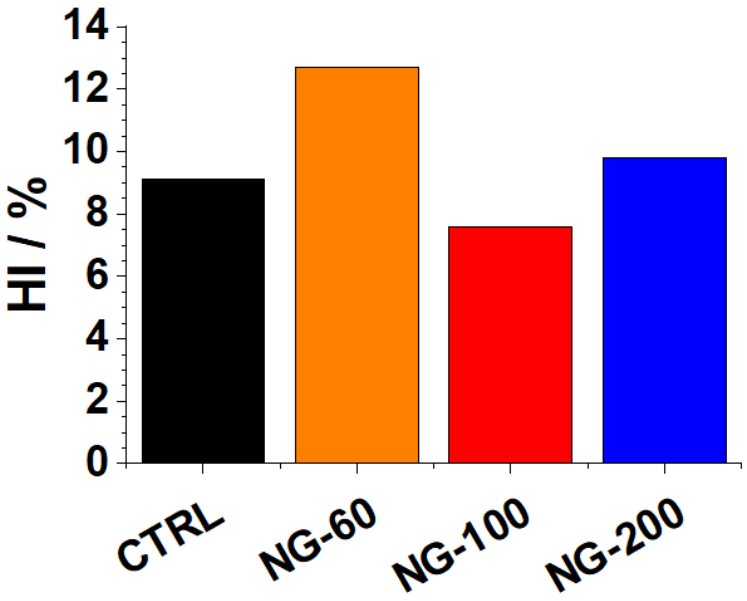

Fig. S19. Hysteresis index for various perovskite/nanogel devices. The hysteresis index was calculated using HI = 100 x (PCE_{Rev} – PCE_{Fwd})/PCE_{Rev}, where PCE_{Rev} and PCE_{Fwd} are the average PCE values from the reverse and forward sweeps (see Table S4).

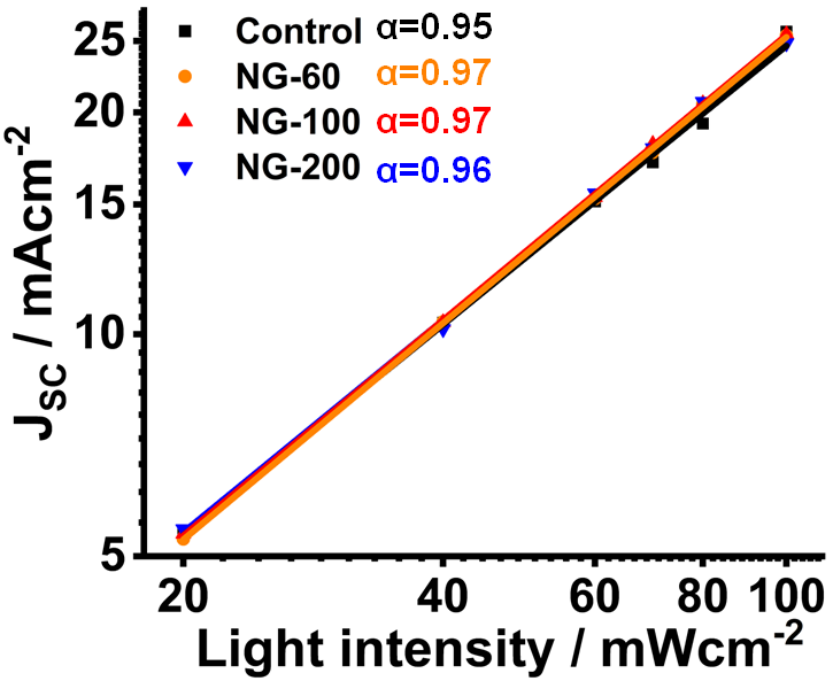

Fig. S20. The variation of the short-circuit current densities with incident light intensity.

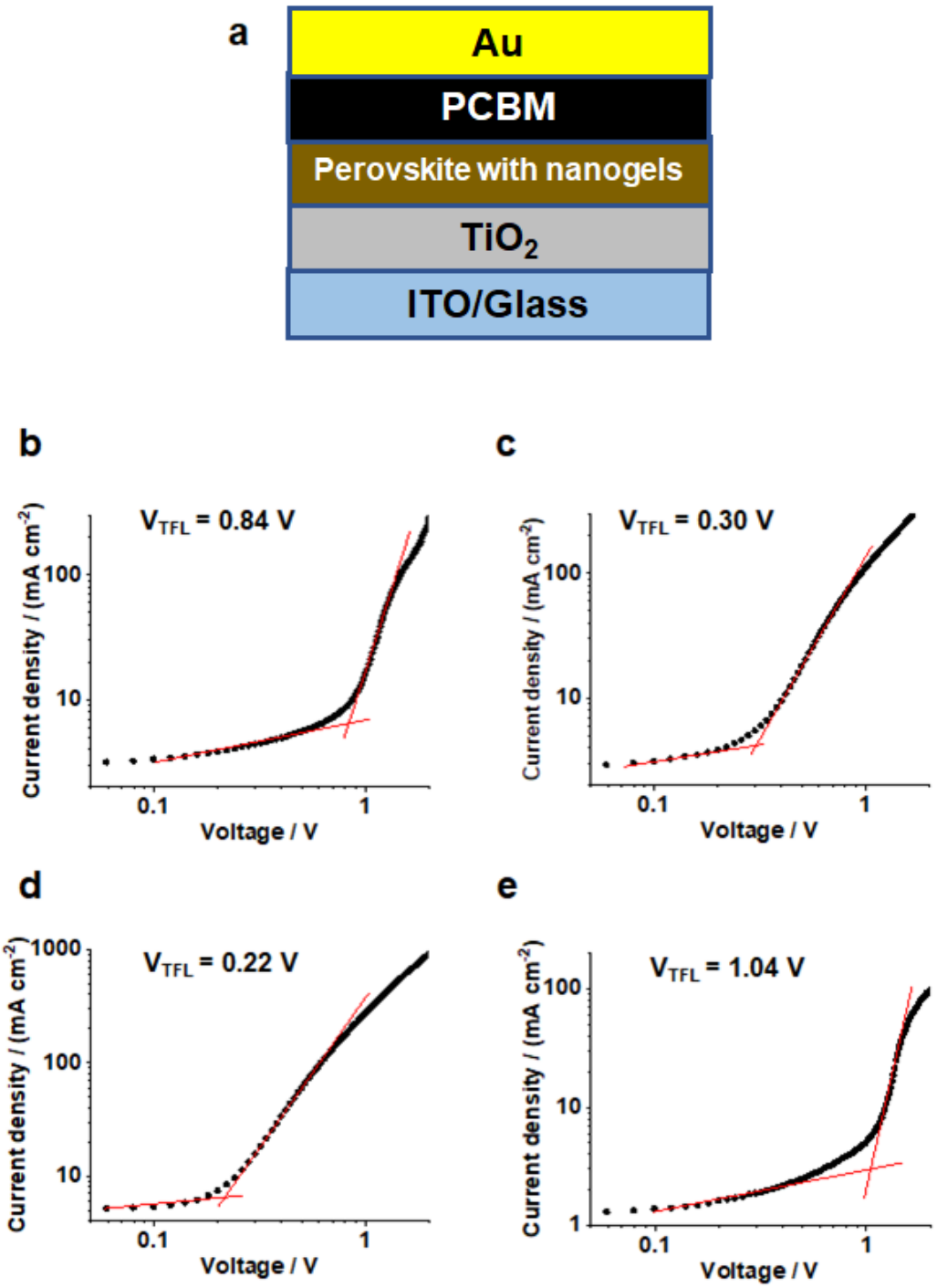

Fig. S21. (a) The architecture of the space-charge-limited current (SCLC) electron-only devices. Data measured from devices prepared using the **(b)** control, **(c)** NG-60, **(d)** NG-100 and **(e)** NG-200 systems. The trap-filled voltages are shown.

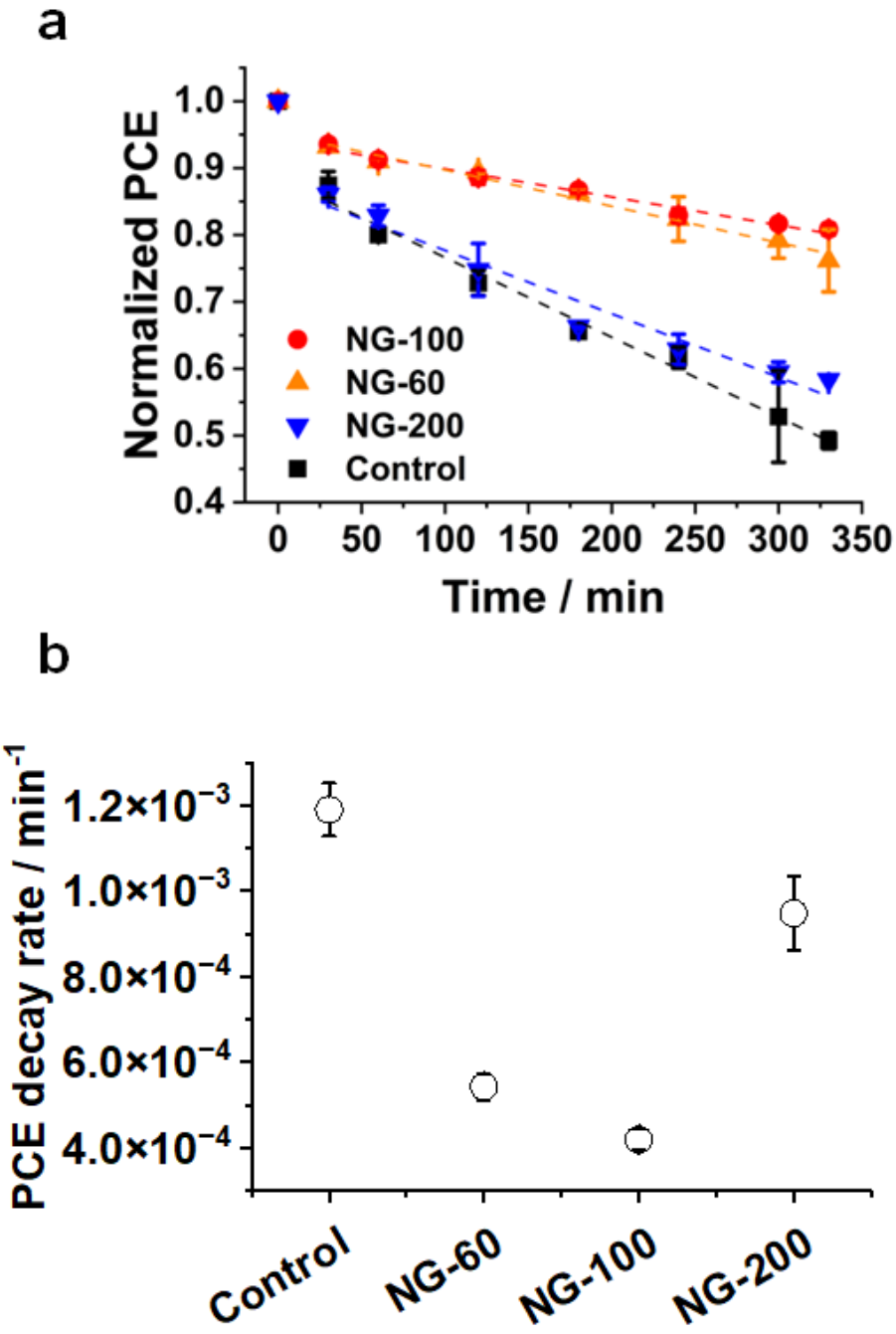

Fig. S22. (a) Light soaking stability measurements of the devices under 1 Sun illumination and 35% RH in ambient air at 30 °C. The devices were *not* encapsulation and did *not* have UV protection. **(b)** PCE decay rates using the gradients from the linear fits shown in (a) for each of the systems. The PCE decay rates increased in the order: NG-100 < NG-60 < NG-200 < control.

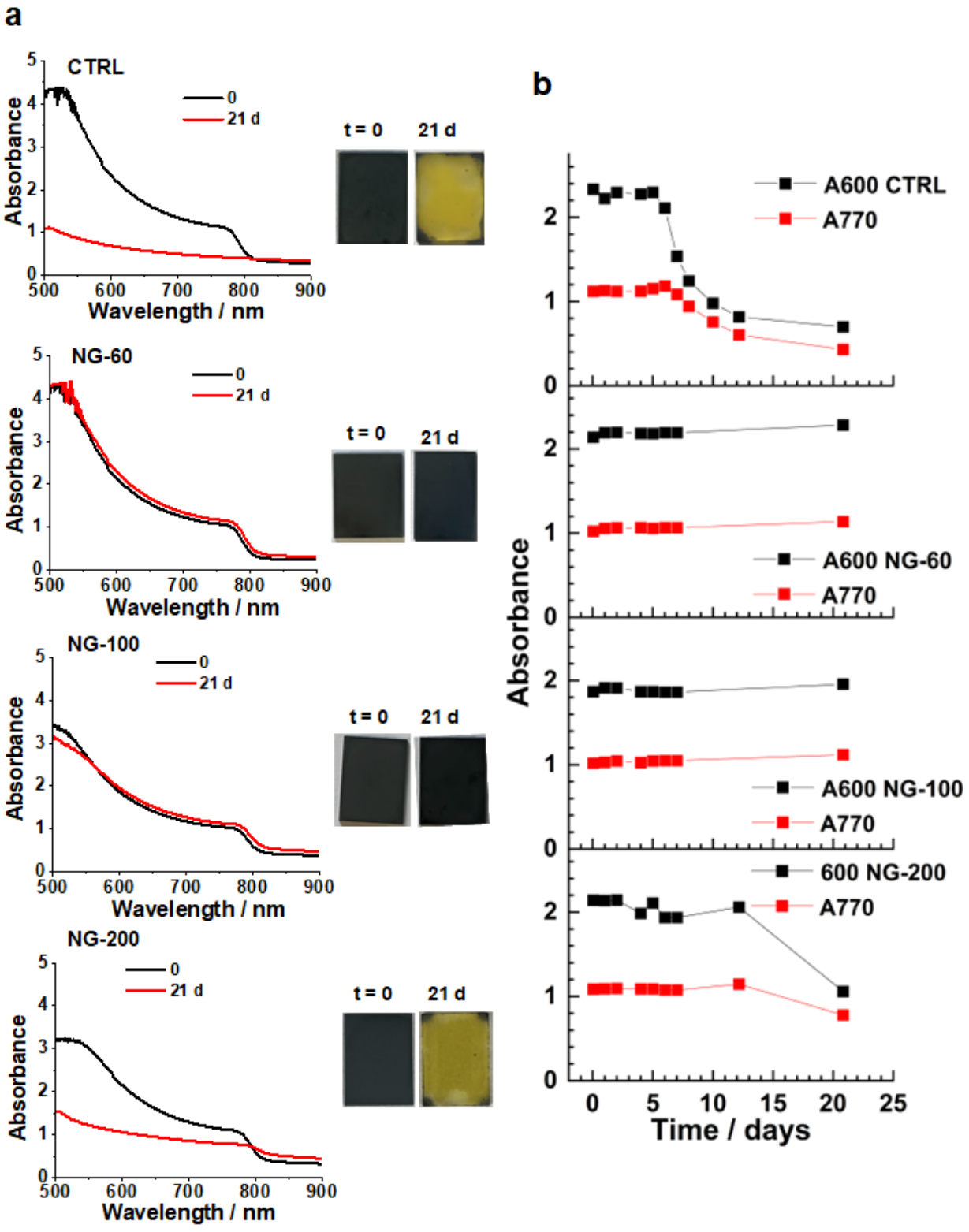

Fig. S23. (a) Shows initial and final UV-visible spectra (after 21 days) and film photographs. **(b)** Variation of absorbance with time measured at 600 and 770 nm. The films were stored at room temperature in the dark within a humid atmosphere (RH = 85% ± 5%).

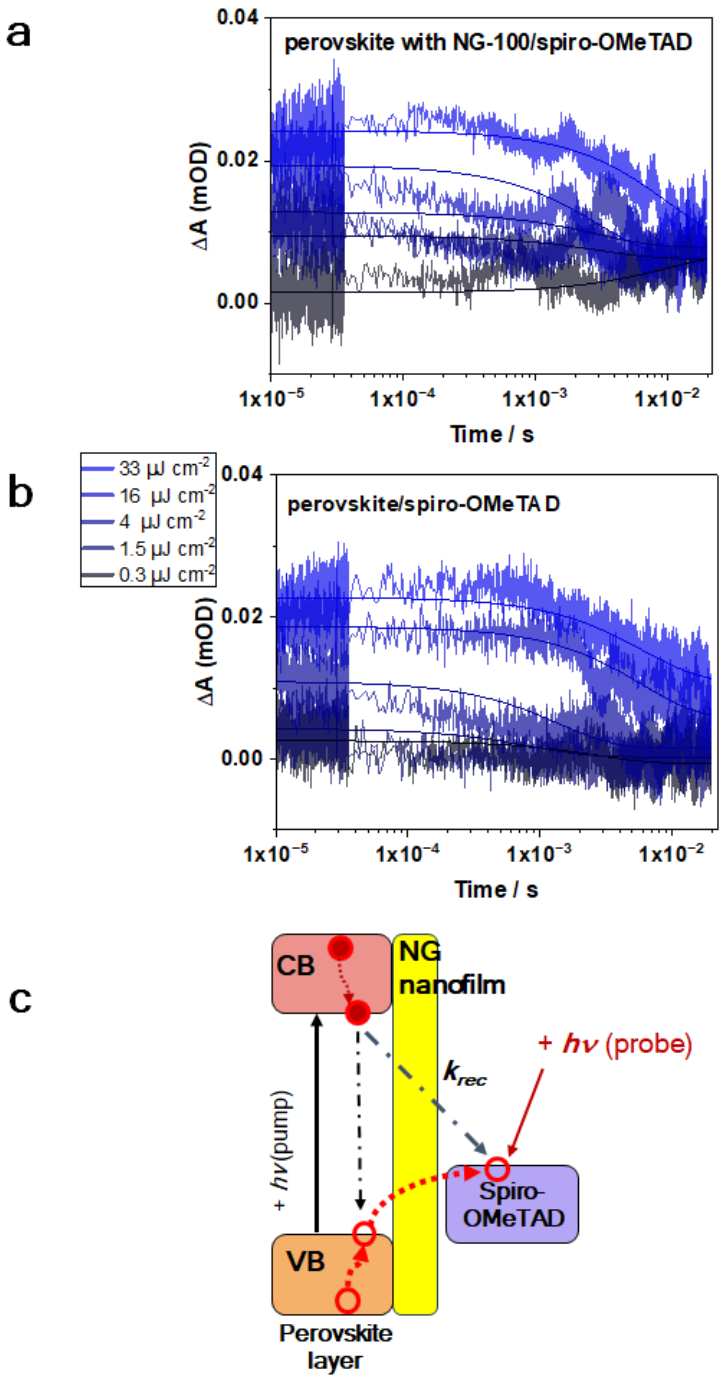

Fig. S24. Transient absorption kinetics of the NG-100 system probed at 1600 nm following a 510 nm pump excitation of the perovskite layer at different excitation densities. **(a)** ITO/TiO_2/perovskite with NG-100/Spiro-OMeTAD and **(b)** control ITO/TiO_2/perovskite/ Spiro-OMeTAD thin films on glass substrates. **(c)** Schematic of the processes underlying TA signal and dynamics. τ_{rec} denotes the recombination lifetime of injected holes at the perovskite-NG/spiro-OMeTAD interface, such that $\Delta OD \propto exp\left[-\left(\frac{t}{\tau}\right)\right]$. The lifetimes from the fitted lines are represented in Table S7.

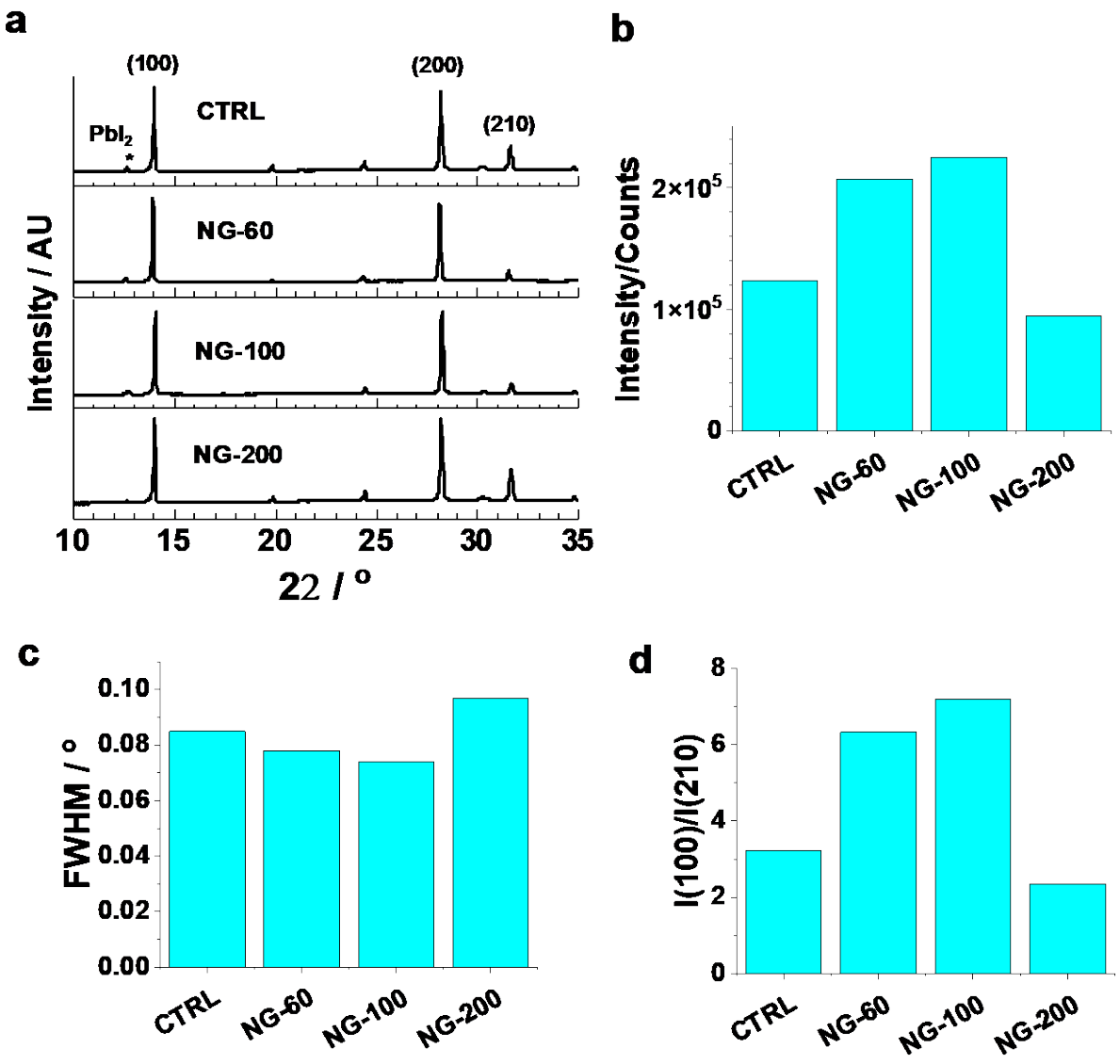

Fig. S25. (**a**) X-ray diffraction patterns for the various films. The peak assignments are taken from the literature[14]. (**b**) Intensity and **(c)** full-width at half maximum height of the (100) peak for all systems and **(d)** ratio of the intensities of the (100) to (210) peaks.

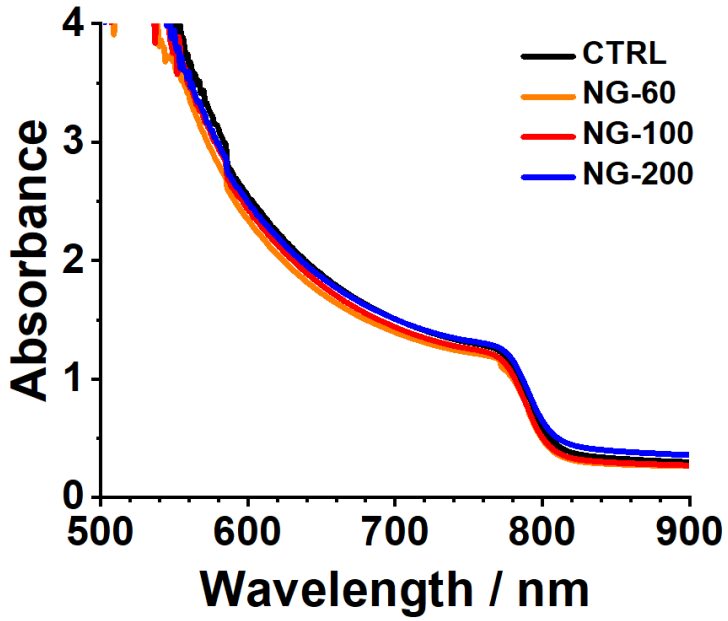

Fig. S26. UV-visible spectra measured for various perovskite films.

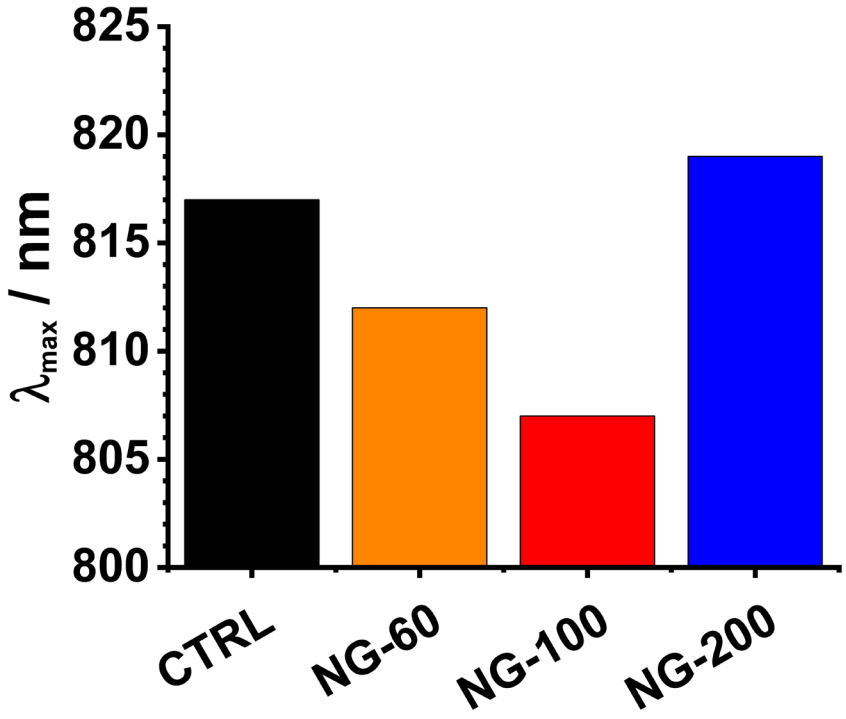

Fig. S27. The wavelength of maximum PL intensity from the PL spectra in Fig. 5a.

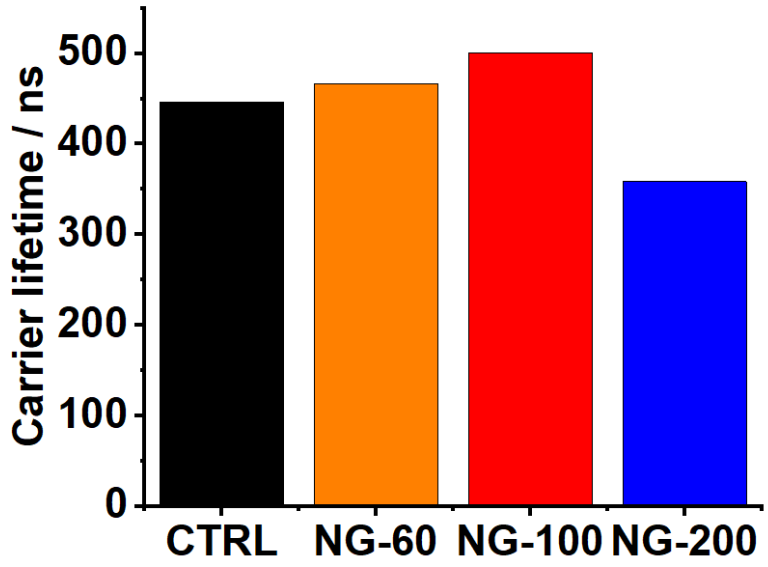

Fig. S28. Average carrier lifetime for various systems. These values were obtained from the data shown in Fig. 5c and equations (3) and (4).

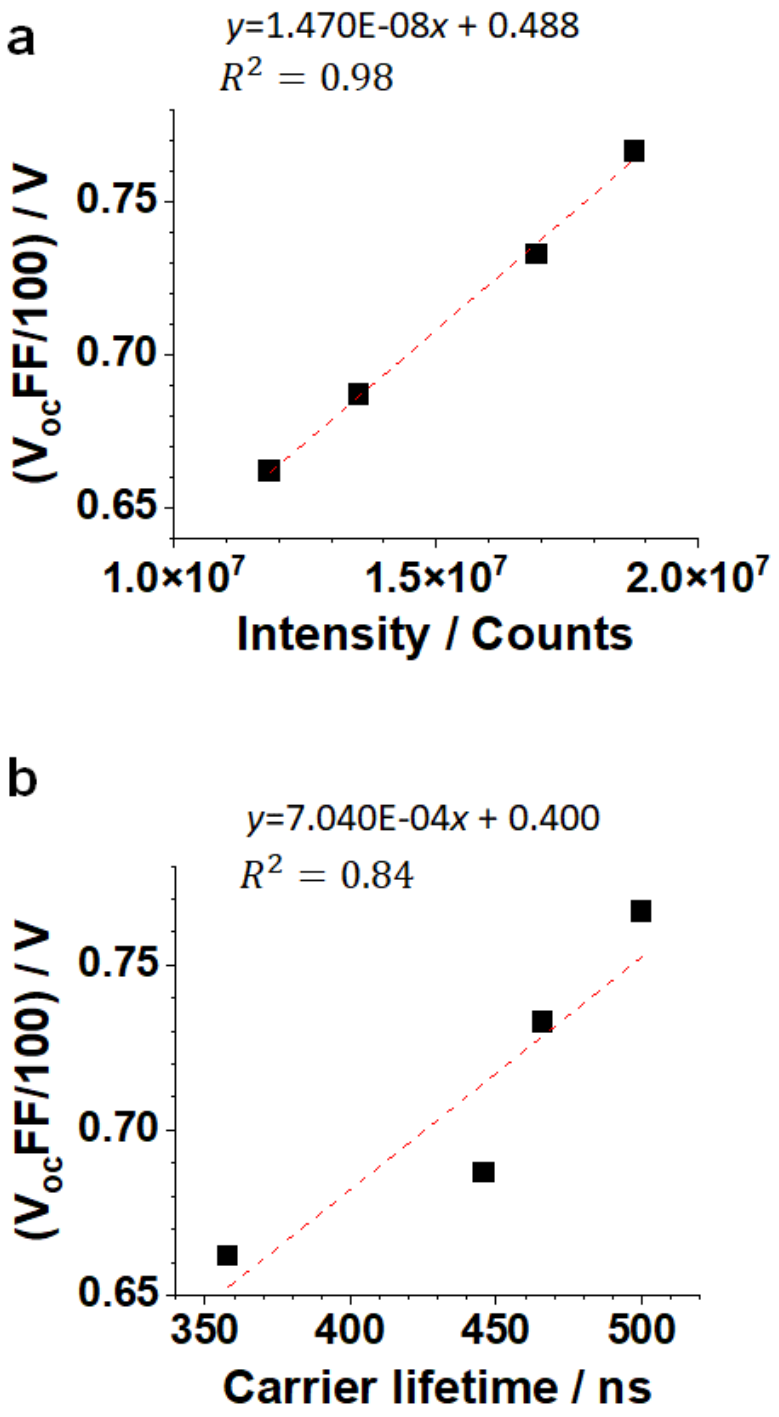

Fig. S29. Variation of the product of V_{oc} and (FF/100) for the devices with the **(a)** steady-state PL intensity and **(b)** carrier lifetime from TRPL measurements. The linear fitting equations are shown.

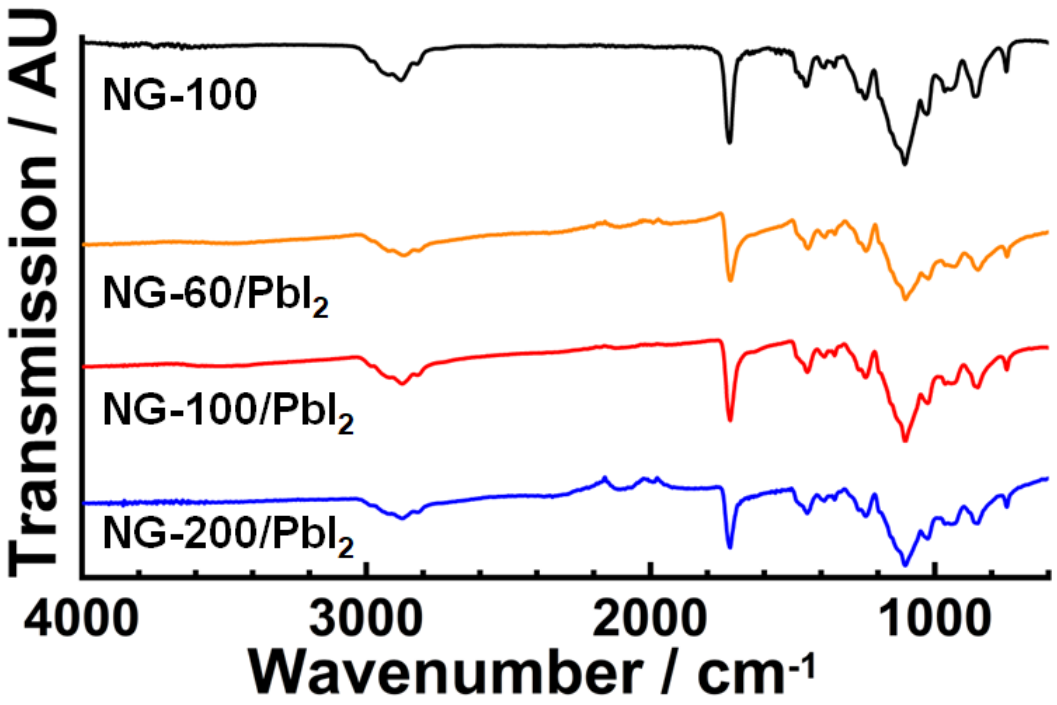

Fig. S30. Full range FTIR spectra for pure NG-100 nanogels and various nanogels mixed with PbI_2.

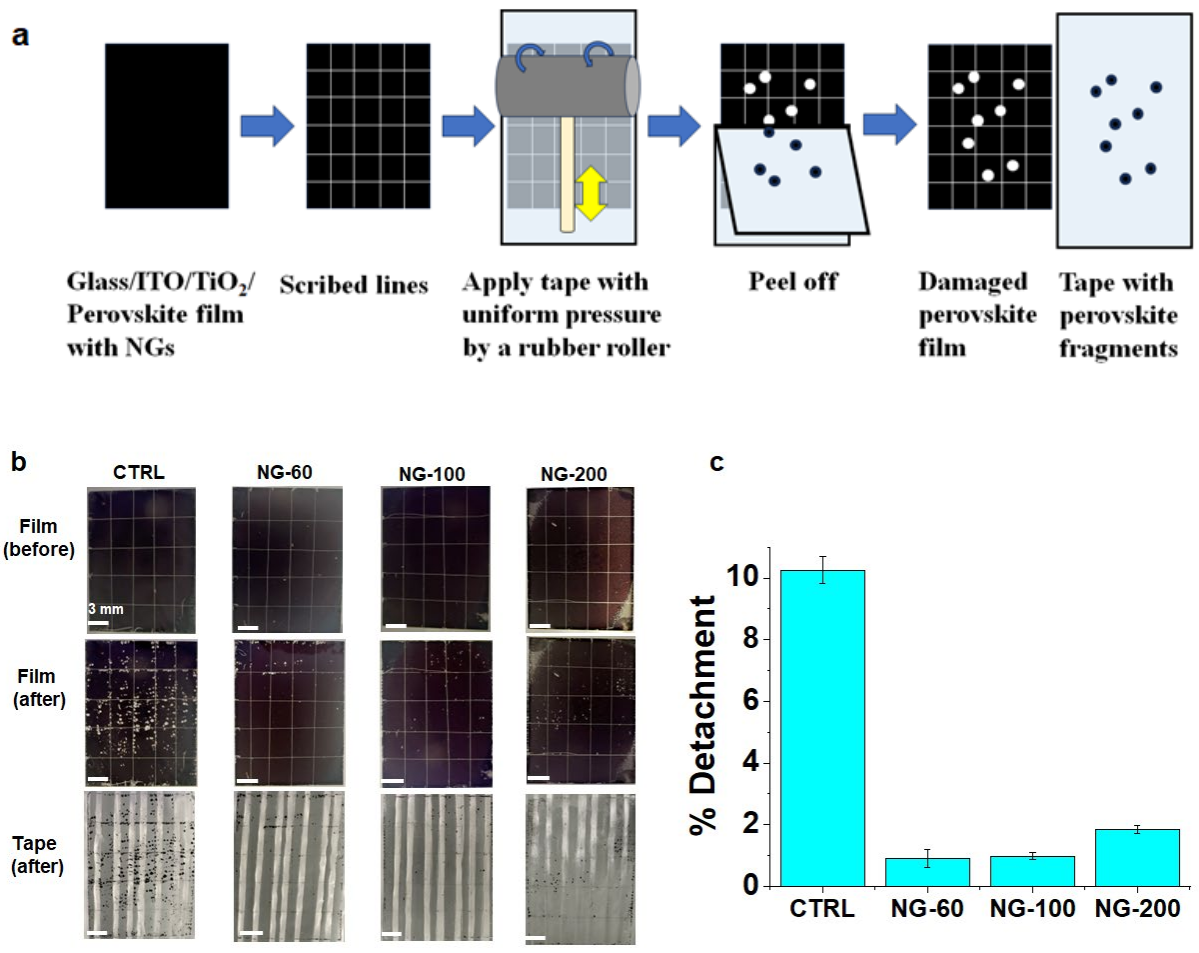

Fig. S31. (a) Depiction of the adhesion strength test. **(b)** Adhesion test results for various films. The top two rows show photographs of the perovskite films before and after the adhesion test. The third row shows photographs of the tape after the adhesion test. **(c)** Measured % detachment of perovskite for the systems. These data were measured from the images shown in the middle row of (b).

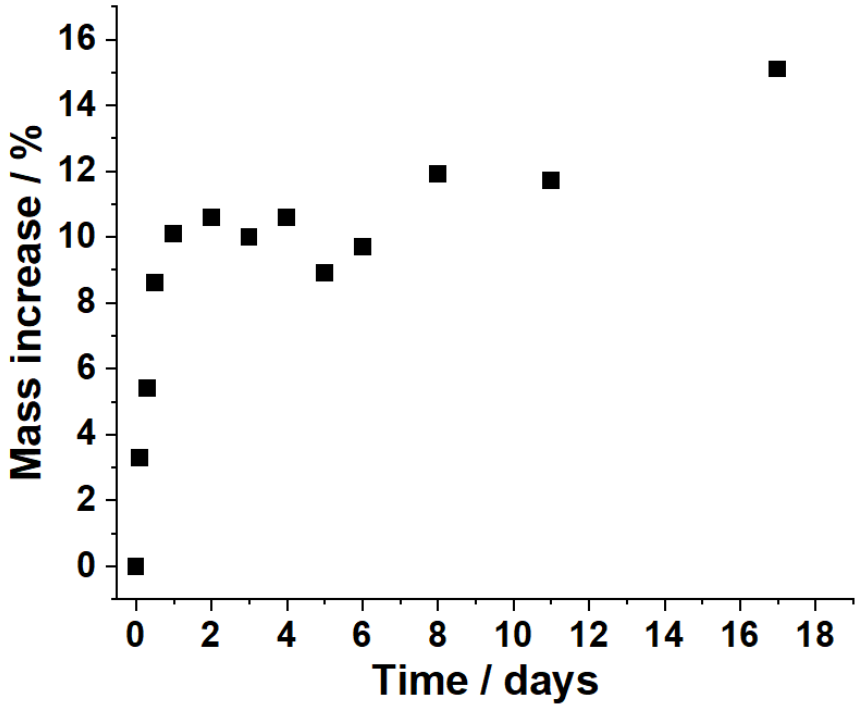

Fig. S32. Mass increase for dried NG-200 pellets with time when placed in a humid environment at room temperature, RH = 95% ± 5%.

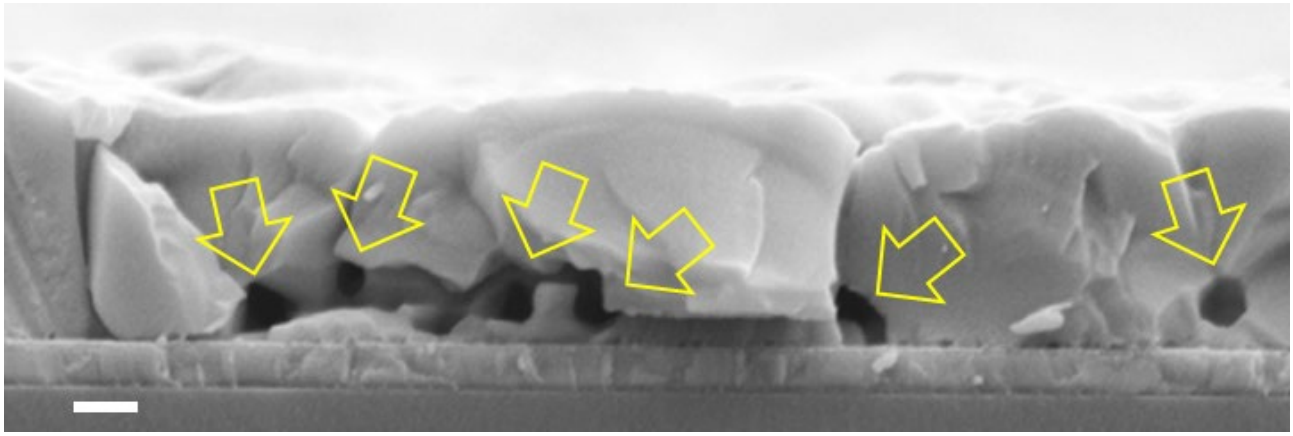

Fig. S33. Representative cross-section SEM image of a perovskite film prepared using 10 mg/g of NG-200 particles. The locations of NG-200 particles that resided at the buried interface are highlighted with arrows. Scale bar: 200 nm.

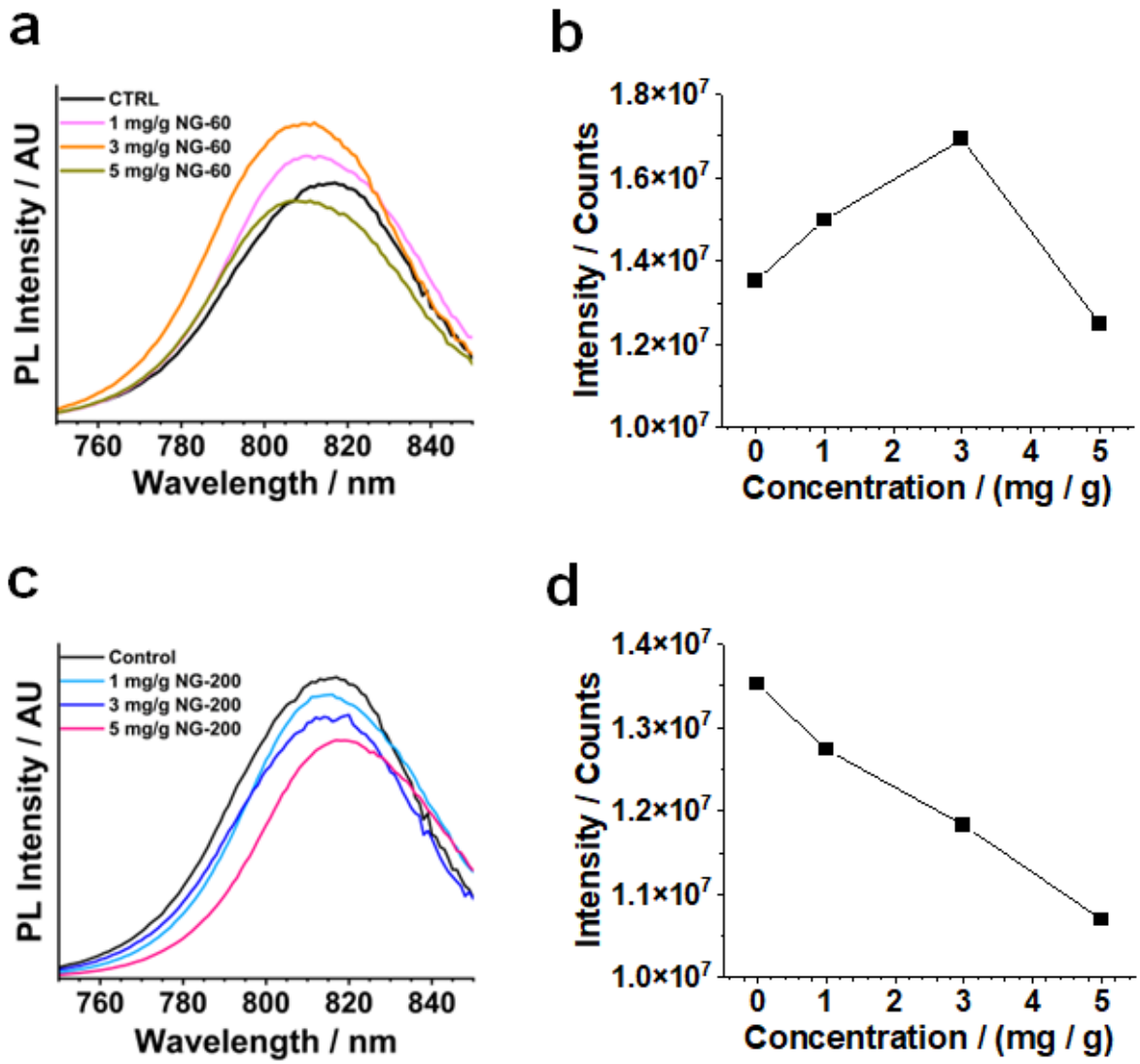

Fig. S34. Effect of NG concentration on PL spectra and maximum PL intensity for **((a)** and **(b))** NG-60 and **((c)** and **(d))** NG-200 systems.

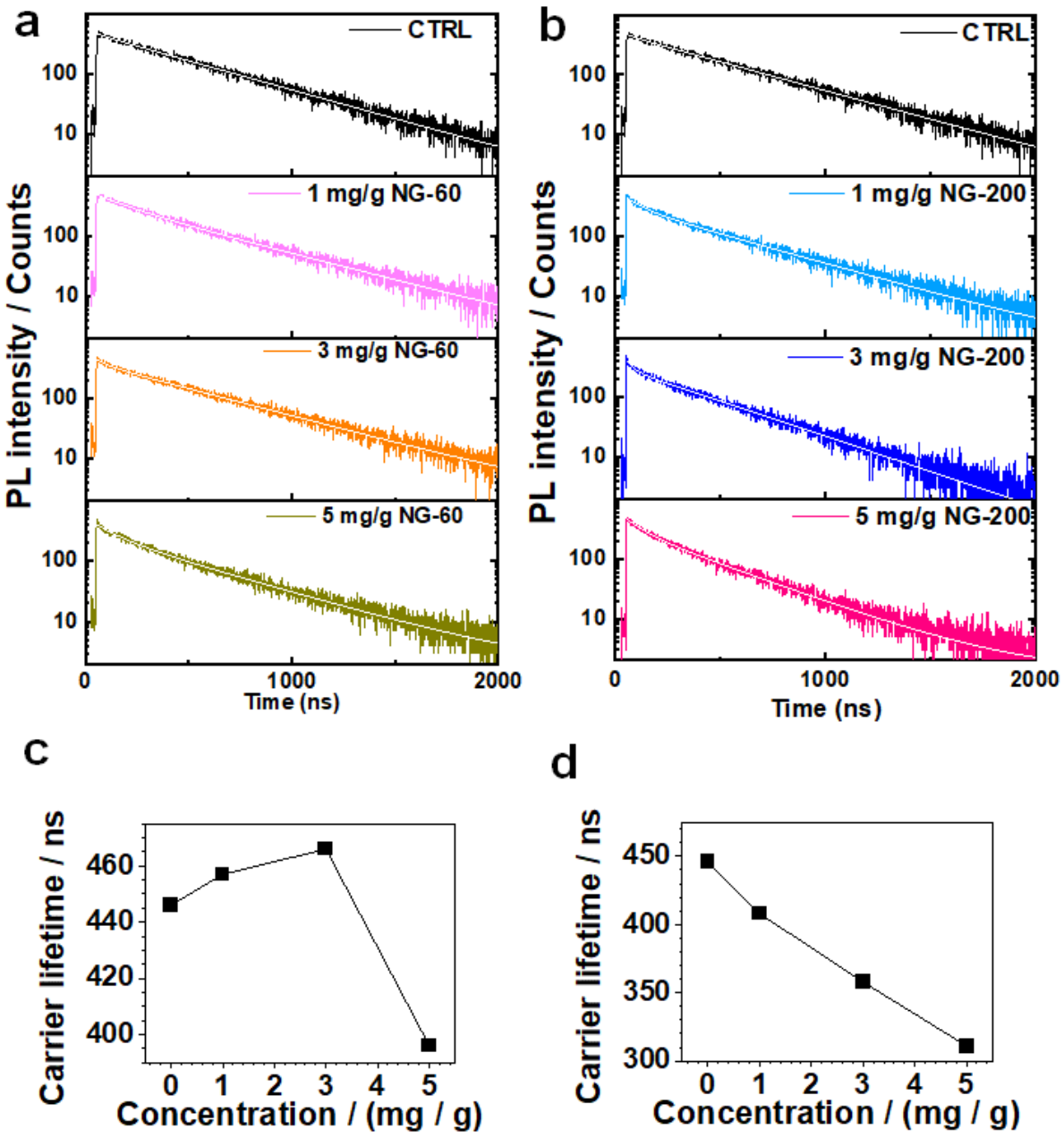

Fig. S35. Effect of NG concentration on TRPL data for **(a)** NG-60 and **(b)** NG-200 systems. **(c)** and **(d)** show the variations of carrier lifetimes for NG-60 and NG-200, respectively, obtained using the fits from figures (a) and (b), respectively.

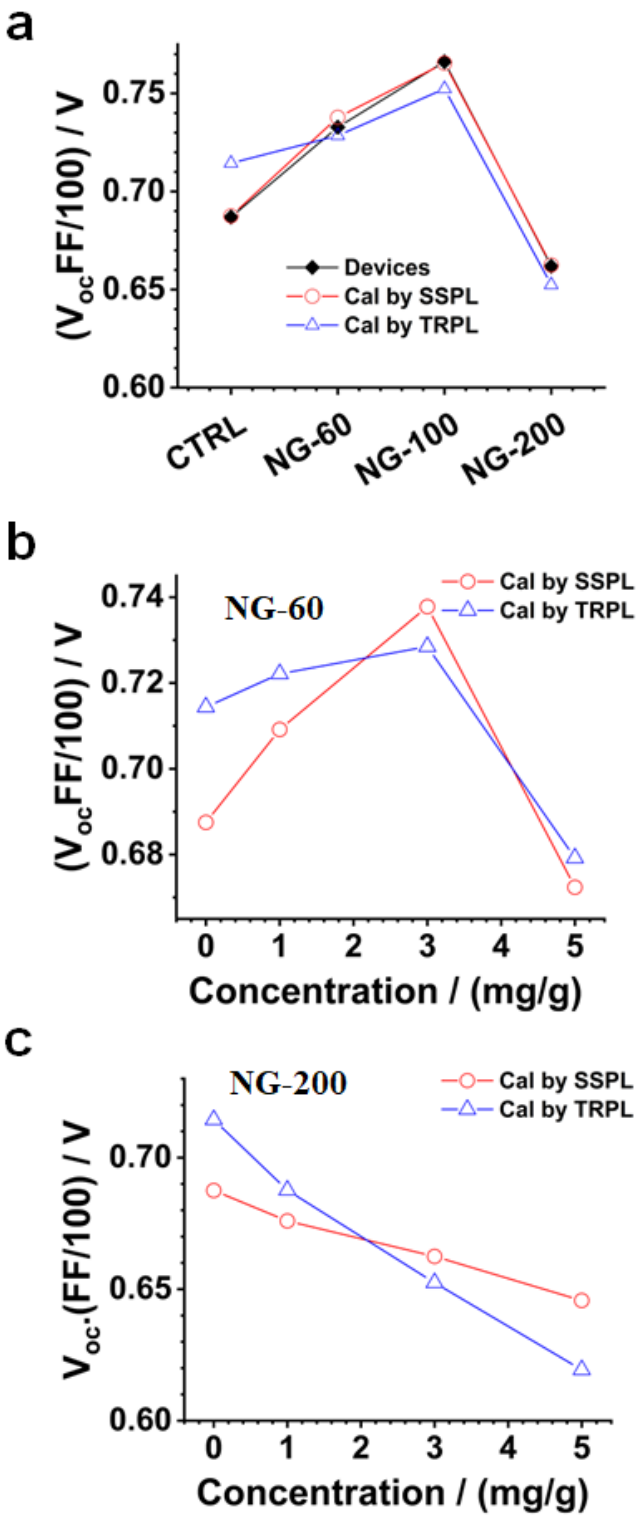

Fig. S36. Calculated and measured (V_{oc}FF/100) values for various systems. The data in **(a)** contain both measured and calculated values. **(b)** and **(c)** show calculated values for NG-60 and NG-200 systems.

TABLES

Table S1. Nanogel synthesis conditions

Nanogel	MEO_2MA/g	EGDMA/g	KPS/mg [a]	SDS/mg [b]	Stirrer blade diameter/mm	Reactor volume/mL
NG-60	1.40	0.015	30	15	52	250
NG-100	2.81	0.030	60	60	75	500
NG-200	22.48	0.25	60	60	75	500

[a] KPS is dissolved in 12 mL water, [b] SDS is dissolved in 120 mL water for NG-60 and 240 mL for NG-100 and NG-200.

Table S2 Characterization data for the nanogels.

Nanogel	D_{SEM} **/ nm** [a]	$d_{z(water,\ 60°C)}$ **/ nm** [b]	$d_{z(DMF,\ 50°C)}$ **/ nm** [c]	**Zeta potential / mV** [d]
NG-60	60 ± 7	33	119	-41.4
NG-100	103 ± 13	53	159	-49.0
NG-200	202 ± 13	160	240	-40.1

[a] Number-average diameter from SEM, [b] Collapsed z-average diameter measured in water at 60°C, [c] Z-average diameter measured for the nanogels swollen in DMF at 50°C, [d] Zeta potential measured in water at 60°C.

Table S3. Precursor solution compositions used to prepare the perovskite films.

Precursor[a]	MACl / g	MAI / g	FAI / g	PbI_2 / g	DMF / g	DMF-nanogels [b] / g	DMSO / g
CTRL	0.015	0.037	0.120	0.461	0.491	0	0.143
NG-60 [1.0 mg/g]	0.015	0.037	0.120	0.461	0.449	0.042 (30)	0.143
NG-60 [3.0 mg/g]	0.015	0.037	0.120	0.461	0.364	0.127 (30)	0.143
NG-60 [5.0 mg/g]	0.015	0.037	0.120	0.461	0.280	0.211 (30)	0.143
NG-100 [3.0 mg/g]	0.015	0.037	0.120	0.461	0.364	0.127 (30)	0.143
NG-100 [10 mg/g]	0.015	0.037	0.120	0.461	0.069	0.422 (30)	0.143
NG-100 [15 mg/g]	0.015	0.037	0.120	0.461	0.111	0.380 (50)	0.143
NG-100 [20 mg/g]	0.015	0.037	0.120	0.461	0.129	0.362 (70)	0.143
NG-200 [1.0 mg/g]	0.015	0.037	0.120	0.461	0.449	0.042 (30)	0.143
NG-200 [3.0 mg/g]	0.015	0.037	0.120	0.461	0.364	0.127 (30)	0.143
NG-200 [5.0 mg/g]	0.015	0.037	0.120	0.461	0.280	0.211 (30)	0.143

[a] The parameter in [] brackets is the target concentration of nanogels in the precursor solution.

[b] The parameter in () brackets is the concentration of nanogels in DMF dispersion in mg/g that was added to the precursor solution.

Table S4. Measured photovoltaic parameters for the PSCs studied.

Particles (Nanogel concentration)	**Scan direction**	V_{oc} **/ Volts**	J_{sc} **/ mA.cm^{-2}**	**FF / %**	**PCE / %**	**HI / %** [a]
CTRL (0 mg/g)	Fwd	0.95 ± 0.02	25.08 ± 0.52	65.74 ± 3.18	15.75 ± 0.64	9.1
	Rev	0.99 ± 0.01	25.04 ± 0.52	69.39 ± 3.79	17.33 ± 0.90	
	Best	1.00	25.60	71.92	18.40	
NG-60 (3 mg/g)	Fwd	0.96 ± 0.03	25.40 ± 0.35	66.48 ± 1.32	16.17 ± 0.66	12.7
	Rev	1.02 ± 0.02	25.36 ± 0.35	71.84 ± 1.31	18.54 ± 0.40	
	Best	1.04	25.83	71.43	19.12	
NG-100 (3 mg/g)	Fwd	1.02 ± 0.01	25.06 ± 0.60	69.18 ± 2.14	17.70 ± 0.38	7.6
	Rev	1.05 ± 0.01	25.06 ± 0.59	72.97 ± 2.20	19.16 ± 0.47	
	Best	1.05	25.34	75.60	20.08	
NG-100 (10 mg/g)	Fwd	0.98 ± 0.01	24.92 ± 0.73	63.23 ± 1.81	15.37 ± 0.65	12.4
	Rev	1.02 ± 0.01	24.88 ± 0.75	69.20 ± 1.62	17.54 ± 0.58	
	Best	0.95	25.65	73.04	17.84	
NG-200 (3 mg/g)	Fwd	0.98 ± 0.01	24.86 ± 0.72	60.84 ± 1.86	14.76 ± 0.71	9.8
	Rev	1.02 ± 0.01	24.79 ± 0.69	64.89 ± 1.82	16.37 ± 0.85	
	Best	1.02	25.97	70.65	18.73	

[a] Hysteresis index = 100 x (PCE_{Rev} – PCE_{Fwd})/PCE_{Rev}

Table S5. Weight percentage of elements obtained from EDX analysis.

Details	Pb / wt.%	I / wt.%	C / wt.%	N / wt.%	Pb / I[a]
CTRL Position 1	35.2	54.8	6.0	4.0	0.64
CTRL Position 2	35.4	55.9	5.1	3.5	0.63
CTRL Position 3	42.2	49.1	4.7	4.0	0.86
NG-60 Position 1	30.1	58.3	6.8	4.8	0.52
NG-60 Position 2	39.5	52.6	4.3	3.7	0.75
NG-60 Position 3	42.4	49.5	4.1	4.0	0.86

[a] Mass ratio of Pb to I.

Table S6. PSC efficiencies reported for devices based on a similar ETL/ perovskite / HTL / electrode device architecture to that used in this work.

Device architecture	V_{OC} [a] / V	J_{SC} [a] / mA.cm^{-2}	FF [a] / %	PCE[a] / %	PCE[b] / %	Ref
FTO/TiO_2/$FAMAPbI_3$/Spiro-OMeTAD/Au	0.992	23.35	75.97	17.59	20.02	15
FTO/TiO_2/$FA_{0.75}MA_{0.25}PbI_3$ /Spiro-OMeTAD/Ag	0.97	17.36	63.84	-	15.51	16
FTO/TiO_2/$FA_{0.7}MA_{0.3}PbI_3$/ Spiro-OMeTAD/Ag	0.99	20.72	69	14.36	17.02	17
FTO/TiO_2/$FA_{0.85}MA_{0.15}PbI_3$ + DFPDA/ Spiro-OMeTAD/Au	1.08	24.69	75.01	20.00	22.21	18
FTO/TiO_2/$FA_{0.85}MA_{0.15}PbI_3$ + NbF_5/Spiro-OMeTAD/Au	1.03	24.45	72.56	18.30	20.56	19
FTO/TiO_2/$FAMAPbI_3$/ Spiro-OMeTAD/Au	1.07	23.38	72	17.98	19.92	20
Average[c]	1.02	22.33	71.40	17.65	19.21	
Standard deviation[c]	0.05	2.81	4.44	2.05	2.47	
ITO/TiO_2/ $FA_{0.75}MA_{0.25}PbI_3$/ Spiro-OMeTAD/Au	1.00	25.60	71.92	18.40	20.08	**This work**

[a] Data for the best control device. [b] PCE for the best modified device. [c] Calculated from the published data.

Table S7. Lifetimes from the monoexponential fitting of the TAS data.

Excitation density ($\mu J\ cm^{-2}$)	$\tau_{NG\text{-}100}$[a] / ms	τ_{CTRL}[b] / ms
33	9.97 ± 0.42	6.02 ± 0.19
16	2.96 ± 0.08	6.00 ± 0.17
4.0	2.99 ± 0.21	2.65 ± 0.08
1.5	2.99 ± 0.29	2.67 ± 0.19
0.3	3.63 ± 0.34	2.67 ± 0.22

[a] Lifetime for the TiO_2/perovskite/NG-100/Spiro-OMeTAD system. [b] Lifetime for the TiO_2/perovskite/Spiro-OMeTAD system.

Table S8. Results from fitting of the TRPL data[a].

System (Nanogel concentration)	τ_1 / **ns**	A_1 / counts	τ_2 / **ns**	A_2 / counts	τ_{avg} [b] / **ns**
CTRL (0 mg/g)	73.0	18.5	449	430.7	446
NG-60 (1 mg/g)	164.5	133.0	494	345.0	457
NG-60 (3 mg/g)	64.4	65.7	476	371.3	466
NG-60 (5 mg/g)	114.2	135.1	434	261.1	396
NG-100 (3 mg/g)	82.3	92.0	519	320.3	500
NG-200 (1 mg/g)	85.0	132.2	436	299.2	408
NG-200 (3 mg/g)	36.5	122.7	371	287.2	358
NG-200 (5 mg/g)	84.7	157.3	341	298.1	311

[a] The data were obtained by fitting equation (3). [b] Average lifetime calculated using equation (4).

References

1. G. Kresse and D. Joubert, *Phys. Rev. B*, 1999, **59**, 1758-1775.
2. G. Kresse and J. Hafner, *Phys. Rev. B*, 1993, **47**, 558-561.
3. G. Kresse and J. Furthmüller, *Phys. Rev. B*, 1996, **54**, 11169-11186.
4. J. P. Perdew, A. Ruzsinszky, G. I. Csonka, O. A. Vydrov, G. E. Scuseria*, et al.*, *Phys. Rev. Lett.*, 2008, **100**, 136406.
5. S. Grimme, J. Antony, S. Ehrlich and H. Krieg, *J. Chem. Phys.*, 2010, **132**.
6. R. Wang, A. Altujjar, N. Zibouche, X. Wang, B. F. Spencer*, et al.*, *Energy Environ. Sci.*, 2023, **16**, 2646-2657.
7. D. Ghosh, A. Aziz, J. A. Dawson, A. B. Walker and M. S. Islam, *Chem. Mater.*, 2019, **31**, 4063-4071.
8. C. Eames, J. M. Frost, P. R. F. Barnes, B. C. O'Regan, A. Walsh*, et al.*, *Nat. Commun.*, 2015, **6**, 7497.
9. The initial molecular structures were obtained from PubChem online database (PubChem Identifier: CID 170752, URL: https://pubchem.ncbi.nlm.nih.gov/compound/170752).
10. E. Aprà, E. J. Bylaska, W. A. de Jong, N. Govind, K. Kowalski*, et al.*, *J. Chem. Phys.*, 2020, **152**.
11. Y.-S. Lin, G.-D. Li, S.-P. Mao and J.-D. Chai, *J. Chem. Theory Comput.*, 2013, **9**, 263-272.
12. D. Lu, M. Zhu, W. Wang, S. Wu, B. R. Saunders*, et al.*, *Soft Matter*, 2019, **15**, 527-536.
13. A. Altujjar, M. Z. Mokhtar, Q. Chen, J. Neilson, B. F. Spencer*, et al.*, *ACS Appl. Mater. Interfaces*, 2021, **13**, 58640-58651.
14. T. A. S. Doherty, S. Nagane, D. J. Kubicki, Y.-K. Jung, D. N. Johnstone*, et al.*, *Science*, 2021, **374**, 1598-1605.
15. K. Jung, J. Lee, C. Im, J. Do, J. Kim*, et al.*, *ACS Energy Lett.*, 2018, **3**, 2410-2417.
16. F. Ji, L. Wang, S. Pang, P. Gao, H. Xu*, et al.*, *J. Mater. Chem. A*, 2016, **4**, 14437-14443.

17. G. Li, T. Zhang, N. Guo, F. Xu, X. Qian*, et al.*, *Angew. Chem., Int. Ed.*, 2016, **55**, 13460-13464.

18. Y. Cai, J. Cui, M. Chen, M. Zhang, Y. Han*, et al.*, *Adv. Funct. Mater.*, 2021, **31**, 2005776.

19. S. Yuan, F. Qian, S. Yang, Y. Cai, Q. Wang*, et al.*, *Adv. Funct. Mater.*, 2019, **29**, 1807850.

20. R. Xia, X.-X. Gao, Y. Zhang, N. Drigo, V. I. E. Queloz*, et al.*, *Adv. Mater.*, 2020, **32**, 2003801.